

AD-A138 966

INTERFACE PROPERTIES OF LATTICE-MATCHED INGAASP/INP  
HETEROJUNCTIONS.. (U) ILLINOIS UNIV AT URBANA DEPT OF  
ELECTRICAL ENGINEERING G E STILLMAN ET AL. AUG 81

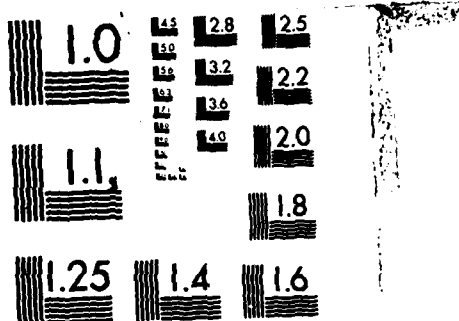
UNCLASSIFIED UILU-ENG-81-2552 N00014-77-C-0653

1/1

F/G 20/12

NL

END  
DATE  
FILED  
4-24-84  
DTIC



MICROCOPY RESOLUTION TEST CHART  
NATIONAL BUREAU OF STANDARDS-1963-A

AD A138966

UILU-ENG-81-2552

1

INTERFACE PROPERTIES OF LATTICE-MATCHED InGaAsP/InP HETEROJUNCTIONS

G. E. Stillman  
and  
M. M. Tashima  
Department of Electrical Engineering  
University of Illinois at Urbana-Champaign  
Urbana, IL 61801

August 1981

Final Report for N00014-77-C-0653  
for period 21 August 1977 - 22 August 1980

Distribution Unlimited

Prepared for

Office of Naval Research  
Arlington, Virginia 22219

ATTN: Larry R. Cooper and George B. Wright

DTIC  
SELECTED  
S MAR 9 1984  
D  
A

The views and conclusions contained in this document are those of the authors and should not be interpreted as necessarily representing the official policies, either expressed or implied, of the Naval Research Laboratory or the U.S. Government.

DTIC FILE COPY

84 03 09 067

UILU-ENG-81-2552

INTERFACE PROPERTIES OF LATTICE-MATCHED InGaAsP/InP HETEROJUNCTIONS

G. E. Stillman  
and  
M. M. Tashima  
Department of Electrical Engineering  
University of Illinois at Urbana-Champaign  
Urbana, IL 61801

August 1981

Final Report for N00014-77-C-0653  
for period 21 August 1977 - 22 August 1980

Distribution Unlimited

Prepared for

Office of Naval Research  
Arlington, Virginia 22219

ATTN: Larry R. Cooper and George B. Wright

The views and conclusions contained in this document are those of the authors and should not be interpreted as necessarily representing the official policies, either expressed or implied, of the Naval Research Laboratory or the U.S. Government.

## UNCLASSIFIED

SECURITY CLASSIFICATION OF THIS PAGE (When Data Entered)

| REPORT DOCUMENTATION PAGE  |   | READ INSTRUCTIONS BEFORE COMPLETING FORM |
|--|---|--|
| 1. REPORT NUMBER   | 2. GOVT ACCESSION NO.   | 3. RECIPIENT'S CATALOG NUMBER            |
|  |   | AD-A138966                               |
| 4. TITLE (and Subtitle)<br>INTERFACE PROPERTIES OF LATTICE-MATCHED<br>InGaAsP/InP HETEROJUNCTIONS  | 5. TYPE OF REPORT & PERIOD COVERED<br>Final Report<br>21 Aug. 1977 - 22 Aug. 1980 |  |
| 7. AUTHOR(s)<br>G. E. Stillman and M. M. Tashima   | 6. PERFORMING ORG. REPORT NUMBER<br>UTLU-ENG-81-2552                              |  |
| 9. PERFORMING ORGANIZATION NAME AND ADDRESS<br>Department of Electrical Engineering<br>University of Illinois at Urbana-Champaign<br>Urbana, Illinois 61801  | 10. PROGRAM ELEMENT, PROJECT, TASK AREA & WORK UNIT NUMBERS                       |  |
| 11. CONTROLLING OFFICE NAME AND ADDRESS<br>Office of Naval Research<br>Arlington, Virginia 22219   | 12. REPORT DATE<br>August 1981  |  |
| 14. MONITORING AGENCY NAME & ADDRESS (if different from Controlling Office)  | 13. NUMBER OF PAGES<br>85 pp.   |  |
| 16. DISTRIBUTION STATEMENT (of this Report)<br>Distribution unlimited.   | 15. SECURITY CLASS. (of this report)  |  |
| 17. DISTRIBUTION STATEMENT (of the abstract entered in Block 20, if different from Report)   |   |  |
| 18. SUPPLEMENTARY NOTES<br>The views and conclusions contained in this document are those of the authors and should not be interpreted as necessarily representing the official policies, either expressed or implied, of the Naval Research Laboratory or the U.S. Government.  |   |  |
| 19. KEY WORDS (Continue on reverse side if necessary and identify by block number)<br>LPE, VPE, InGaAs, InGaAsP, InP, lattice mismatch, X-ray diffraction, minority carrier diffusion length   |   |  |
| 20. ABSTRACT (Continue on reverse side if necessary and identify by block number)<br>The growth of InGaAsP and InGaAs by liquid phase epitaxy (LPE) on InP substrates has been investigated to obtain the optimum crystal growth parameters to produce high quality epitaxial layers. The lattice mismatch of these layers with respect to the underlying InP substrate was determined by X-ray diffraction, and the energy gap was obtained by optical spectrophotometer transmission measurements. The distribution coefficients for the growth of lattice matched InGaAsP in the 1.15 to 1.31 $\mu$ m spectral region were determined. The surface morphology of the epitaxial layers was found |   |  |

DD FORM 1 JAN 1973 EDITION OF 1 NOV 63 IS OBSOLETE

UNCLASSIFIED

SECURITY CLASSIFICATION OF THIS PAGE (When Data Entered)

SAC-60

## TABLE OF CONTENTS

|  | Page |
|--|------|
| I. INTRODUCTION. . . . .                                       | 1    |
| II. X-RAY DIFFRACTION . . . . .                                | 2    |
| A. Crystal Lattices. . . . .                                   | 2    |
| B. Production of X-Rays. . . . .                               | 2    |
| C. Diffraction . . . . .                                       | 4    |
| D. X-ray Diffractometer and Alignment. . . . .                 | 5    |
| E. X-ray Detection System. . . . .                             | 7    |
| F. Typical Diffraction Curves. . . . .                         | 11   |
| G. Absorption Effects. . . . .                                 | 13   |
| III. EXPERIMENTAL RESULTS - LPE GROWTH . . . . .               | 16   |
| A. Crystal Growth. . . . .                                     | 16   |
| B. Determination of Distribution Coefficients. . . . .         | 19   |
| C. Effects of Lattice Mismatch on Surface Morphology . . . . . | 23   |
| D. Variation of Melt Composition . . . . .                     | 23   |
| E. Effect of Growth Temperature. . . . .                       | 29   |
| F. Effect of Growth Technique. . . . .                         | 33   |
| 1. Super cooling . . . . .                                     | 33   |
| 2. Equilibrium cooling . . . . .                               | 35   |
| G. Effect of Growth Solution Dopants . . . . .                 | 35   |
| H. Interfacial Grading . . . . .                               | 41   |
| 1. Auger depth profiling . . . . .                             | 41   |
| 2. Effect of lattice mismatch. . . . .                         | 41   |
| 3. Effect of dissolution . . . . .                             | 46   |
| IV. MINORITY CARRIER DIFFUSION LENGTHS. . . . .                | 49   |
| A. Introduction. . . . .                                       | 49   |
| B. Theory of the Measurement . . . . .                         | 49   |
| C. Experimental Procedures . . . . .                           | 57   |
| 1. Crystal growth. . . . .                                     | 57   |
| 2. Wafer processing. . . . .                                   | 58   |
| 3. Diffusion length measurement system . . . . .               | 61   |
| D. Experimental Results. . . . .                               | 68   |
| 1. Effect of lattice mismatch. . . . .                         | 68   |
| 2. Effect of hole concentration. . . . .                       | 68   |
| 3. Effect of the source temperature on $L_p$ of VPE InP . . .  | 71   |

|  | Page |
|--|------|
| V. DISCUSSION AND CONCLUSIONS. . . . .                     | 74   |
| A. Characterization of LPE Growth. . . . .                 | 74   |
| B. Minority Carrier Diffusion Lengths. . . . .             | 75   |
| REFERENCES. . . . .  | 77   |
| APPENDIX: PUBLICATIONS SUPPORTED BY THIS CONTRACT. . . . . | 79   |

Accession For

|               |                                     |
|---------------|-------------------------------------|
| NTIS GR&I     | <input checked="" type="checkbox"/> |
| DTIC TAB      | <input type="checkbox"/>            |
| Unannounced   | <input type="checkbox"/>            |
| Justification |                                     |

By

|                    |  |
|--------------------|--|
| Distribution/      |  |
| Availability Codes |  |

|      |                         |
|------|-------------------------|
| Dist | Avari and/or<br>Special |
| A1   |                         |

*Approved*

## LIST OF FIGURES

| Figure  | Page |
|---|------|
| 1. Plan view of the single crystal diffractometer used in this work. . . . .  | 6    |
| 2. Block diagram of the X-ray detection system . . . . .  | 8    |
| 3. The count rate vs. SCA voltage with a 0.1 V $\Delta E$ setting for the Cu $K\alpha_1$ line . . . . .   | 10   |
| 4. Typical intensity vs. Bragg angle diffraction curves for the (600), (400), and (200) reflections from a polished (100)-InP crystal. . . . .  | 12   |
| 5. Diffraction curves for the (442) and (333) reflections from an InGaAs layer which is lattice mismatched to the (111)-InP substrate showing the effects of absorption and secondary extinction. . . . . | 15   |
| 6. Temperature-time growth programs used in this work. . . . .  | 17   |
| 7. Distribution coefficients as a function of $y$ , the As composition of the grown layer. . . . .  | 20   |
| 8. (600) diffraction curves for layers of various solid compositions. . . . .   | 22   |
| 9. (600) diffraction curves for four samples grown from melts with differing amounts of As. . . . .   | 25   |
| 10. The variation of lattice mismatch and bandgap wavelength with the atomic fraction of As in the melt. . . . .  | 26   |
| 11. The variation of lattice mismatch and bandgap wavelength with the atomic fraction of Ga in the melt. . . . .  | 27   |
| 12. The variation of lattice mismatch and bandgap wavelength with the atomic fraction of P in the melt . . . . .  | 28   |
| 13. (600) diffraction curves for three quaternary layers grown at three different temperatures: (a) 635°C, (b) 640°C, and (c) 645°C. . . . .  | 30   |
| 14. The variation of lattice mismatch and bandgap wavelength with the growth temperature for the step cooling growth technique . . . . .  | 31   |

| Figure  | Page |
|---|------|
| 15. (600) single and double crystal diffraction curves for a step cooled and a super cooled sample. Curves (a) and (c) are for the step cooled sample measured with single and double crystal diffractometer, respectively. Curves (b) and (d) are for the super cooled sample measured with a single and double crystal diffractometer, respectively. . . . .  | 32   |
| 16. (600) diffraction curves for samples grown with an initial supersaturation of 10°C and cooling rates R of (1) 0, (2) 0.25, (3) 0.40, and (4) 0.80°C/min . . . . .   | 34   |
| 17. (600) diffraction curves of an InGaAsP layer grown by the equilibrium cooling technique after the layer was etched for progressively longer times from (a) to (d). Curve (a) is for the as grown 4.0 $\mu\text{m}$ thick layer ( $\Delta a/a = 0.06\%$ ), (b) after 1.5 $\mu\text{m}$ has been etched ( $\Delta a/a = -0.04\%$ ), (c) after 2.1 $\mu\text{m}$ was etched ( $\Delta a/a = -0.09\%$ ), and (d) after 2.7 $\mu\text{m}$ was etched ( $\Delta a/a = -0.13\%$ ). . . . . | 36   |
| 18. Variation of the lattice mismatch as a function of the amount of the layer that has been removed. The labeled points correspond to the curves in Fig. 17. . . . .   | 37   |
| 19. The variation of the lattice mismatch and transmission measurement wavelength, $\lambda_T$ , as a function of $X_{\text{Te}}^\lambda$ . . . . .   | 39   |
| 20. The variation of the lattice mismatch and $\lambda_T$ as a function of $X_{\text{Zn}}^\lambda$ for two different melt compositions. . . . .   | 40   |
| 21. Auger depth profile of an InGaAsP/InP/InGaAsP heterostructure where the $\lambda_g = 1.15 \mu\text{m}$ quaternary is closely lattice matched to the InP. . . . .  | 43   |
| 22. Auger profile of an InGaAsP/InP/InGaAsP heterostructure where the lattice mismatch between the quaternary and InP is - 0.11%. . . . .   | 44   |
| 23. Auger profile of an InGaAsP/InP/InGaAsP heterostructure where the lattice mismatch is +0.20%. . . . .   | 45   |
| 24. Auger profile of an InGaAsP/InGaAs/InGaAsP heterostructure showing the effects of dissolution at the InGaAsP/InGaAs interface . . . . .   | 47   |
| 25. The circuit model used to calculate the solution for the short circuit current due to minority carrier diffusion . . . . .  | 50   |
| 26. Effect of the diffusion length on the short circuit current . . . . .   | 52   |
| 27. Effect of surface recombination on the short circuit current . . . . .  | 53   |

| Figure  | Page |
|---|------|
| 28. Effect of the absorption coefficient on the short circuit current . . . . .   | 54   |
| 29. Effect of the minority carrier diffusivity on the short circuit current . . . . .   | 55   |
| 30. An optical micrograph of the angle-lapped surface of an InGaAs epitaxial layer. . . . .   | 60   |
| 31. A pictorial representation of a sample used for the diffusion length measurement. . . . .   | 62   |
| 32. The Dektak surface profilometer scan of the sample in Fig. 30 used to determine the bevel angle, $\theta$ . . . . .   | 63   |
| 33. Schematic diagram of the diffusion length measurement system described in the text. . . . .   | 64   |
| 34. A plot of the logarithm of the normalized photocurrent versus light spot position produced by a typical diffusion length scan. The diffusion length determined from this scan (the dashed line) was $L_p = 1.5 \mu\text{m}$ . . . . . | 67   |
| 35. The variation of the hole diffusion length with lattice mismatch for InGaAsP ( $\lambda_g = 1.15 \mu\text{m}$ ) . . . . .   | 69   |
| 36. The variation of the electron diffusion length with hole concentration of InGaAsP ( $\lambda_g = 1.15 \mu\text{m}$ ) . . . . .  | 70   |
| 37. The variation of the electron diffusion length with hole concentration of InGaAs. Also shown is the hole diffusion length of an n-type InGaAs layer. . . . .  | 72   |
| 38. The effect of In boat source temperature on the hole diffusion lengths of VPE InP epitaxial layers . . . . .  | 73   |

## I. INTRODUCTION

The quaternary semiconductor alloy, InGaAsP, is technologically important because it can be grown lattice matched on readily available InP substrates with a direct energy gap which can be varied continuously in the wavelength region from 0.95  $\mu\text{m}$  (InP) to 1.68  $\mu\text{m}$  ( $\text{In}_{0.53}\text{Ga}_{0.47}\text{As}$ ).<sup>1</sup> Semiconductor optoelectronic devices that can operate in this spectral region are well suited to fiber optic communication systems because optical fibers have their lowest loss and wavelength dispersion in this spectral range<sup>2</sup>. Since the composition of an InGaAsP epitaxial layer can be adjusted to obtain lattice match for a desired band gap energy, these two fundamental parameters and their relations to the crystal growth conditions must be characterized thoroughly in order to obtain the high quality epitaxial layers required for fabricating high performance optoelectronic devices.

In this work, we report on the use of X-ray diffraction in the characterization of InGaAsP grown by liquid phase epitaxy (LPE) since it is the most sensitive means of detecting lattice mismatch<sup>3</sup>. In addition, we have performed minority carrier diffusion length measurements on LPE InGaAsP and InGaAs and have studied the influence of lattice mismatch and majority carrier concentration on the diffusion lengths for these layers. This report is divided into two parts, the first dealing with the applications of X-ray diffraction to characterize the crystal growth and the second treating the minority carrier diffusion length measurements. Before covering the details of the growth characterization section, an introductory discussion of X-ray diffraction is presented to establish the terminology and provide for an understanding of the X-ray diffraction system that was used in this work.

## II. X-RAY DIFFRACTION

### A. Crystal Lattices

The fundamental property of a semiconductor crystal is the three-dimensional periodicity of its constituent atoms. The periodic arrangement of the atoms in the crystal can be referenced to a mathematical construct called a point lattice or more simply lattice, which is defined as a set of points in space that are arranged in a manner where each point has identical surroundings. The building block of the lattice is the unit cell which is a parallelepiped with edges  $\vec{a}_1$ ,  $\vec{a}_2$ , and  $\vec{a}_3$ , and when translated by the lattice vectors,  $\vec{r} = x\vec{a}_1 + y\vec{a}_2 + z\vec{a}_3$  for all integral combinations of x, y, and z fills the entire lattice.

The lattice points generated by  $\vec{r}$  can be grouped in such a way as to produce an infinite set of parallel equidistant planes, (lattice planes) containing every point of the lattice. Each set of lattice planes is uniquely specified by a group of three integers  $(hkl)$  called the indices which are obtained from the reciprocal intercepts the plane closest to the origin of the unit cell makes with the three axes. A plane parallel to an axis is considered to have an intercept at infinity, thus, the reciprocal intercept is 0. The perpendicular distance between two adjacent planes is called the interplanar spacing and is denoted by the notation  $d_{hkl}$ .

### B. Production of X-rays

The source of X-rays for diffraction is an X-ray tube, which is an evacuated envelope containing a tungsten filament cathode as the source of electrons and a water cooled anode which houses the target metal. The X-rays produced at the target pass through ports made of thin beryllium foil which is nearly transparent to X-rays.

The electrons emitted from the heated filament are accelerated to the target through the voltage (~20 kV) applied between the cathode and anode. The highly energetic electrons hitting the target generate a spectrum of X-ray radiation consisting of two components, (1) continuous or white radiation which is due to the deceleration of electrons that hit the target and (2) characteristic radiation which occurs for accelerating voltages greater than a minimum voltage called the critical potential.

The characteristic radiation spectrum is a unique property of the material comprising the target. The characteristic lines of the spectrum are produced when electrons of sufficient energy impinging on the target can knock out an inner shell electron of a target atom leaving the atom in an excited state. One of the ways the atom can return to its ground state is for an outer shell electron to fall into the vacancy of the inner shell and produce an X-ray photon with an energy given by the difference in energy between the inner and outer shells. The shells of an atom are designated by the letters K, L, M, ... beginning with the innermost shell. X-rays produced by an electron of an outer shell falling into a K shell vacancy are called K X-rays and are further labelled by the particular outer shell the electron originally came from. The X-ray line produced from a transition from the M to K shell is called K $\beta$  radiation and the transition of an L to a K shell produces K $\alpha$  emission. The K $\alpha$  radiation is further subdivided into two wavelengths K $\alpha_1$  and K $\alpha_2$  due to the existence of two closely spaced L states involved in the transition to the K level. These characteristic emissions are the ones used for diffraction because they are extremely intense and nearly monochromatic. The wave-

lengths of these lines for the Cu target used in this work are as follows:

$K\beta = 1.39217 \text{ \AA}$ ,  $K\alpha_1 = 1.54051 \text{ \AA}$ , and  $K\alpha_2 = 1.54433 \text{ \AA}$ .

### C. Diffraction

Diffraction is the result of the interaction between the incident X-ray beam and the atoms of the lattice. The oscillating electromagnetic field of the X-ray beam causes the electrons of the atoms to vibrate and emit secondary radiation in all directions, however, only those particular directions where the reemitted radiation from different lattice planes differ in phase by an integral number of wavelengths will there be constructive interference producing an intense diffracted beam. Although the electron density of an atom in a lattice plane is distributed, the secondary radiation from the distribution can be summed to produce a resultant as if the radiation came from the lattice plane. This affects only the intensity and not the direction of the diffracted beam.

The condition for diffraction is given by Bragg's law:

$$n\lambda = 2d \sin \theta$$

where  $\lambda$  is the wavelength of incident radiation,  $d$  is the interplanar spacing of the set of lattice planes under consideration,  $\theta$  is the angle that the incident and diffracted beams make with respect to the lattice planes, and the factor  $n$  is an integer called the order of reflection which arises from the condition that the path difference between the X-rays from different planes be an integral number.

The semiconductor alloys studied in this work belong to the cubic system, therefore, Bragg's law can be rewritten with the interplanar spacing explicitly stated for the cubic lattice:

$$n\lambda = 2 \frac{a_i}{\sqrt{h^2 + k^2 + l^2}} \sin \theta$$

where  $h$ ,  $k$ , and  $l$  are the indices of the diffracting set of planes, and  $a_i$  is the lattice parameter of the cubic unit cell of the crystal  $i$ . This form of Bragg's law emphasizes the fact that, for a particular wavelength, the diffraction directions,  $\theta$ , are uniquely determined by the size and shape of the unit cell.

#### D. X-ray Diffractometer and Alignment

The lattice mismatch of the epitaxial layers was measured with a single crystal diffractometer shown schematically in the plan view of Fig. 1. The focal spot of the X-ray tube, the point at which the X-rays are emitted, and the receiving slit, which defines the width of the diffracted beam entering the detector lie on the diffractometer circle. The sample is mounted on the rotation axis of the diffractometer, and when a diffraction scan is made, the crystal is rotated at one half the angular velocity of the detector to maintain the symmetric Bragg diffraction geometry where the incident angle,  $\theta$ , equals the diffracted angle,  $\theta$ . The angular position of the detector is thus  $2\theta$ , with the zero position defined where focal spot, sample surface, and receiving slit are all in line.

The X-ray beam is collimated by a set of slits located near the exit port of X-ray tube and the receiving slit. These collimators improve the angular resolution of the diffractometer by removal of the divergent X-ray beams which would allow diffraction to occur over a wider range of angles. The Soller slits are composed of a set of thin closely spaced metal plates mounted parallel to the plane of the diffractometer that eliminate the

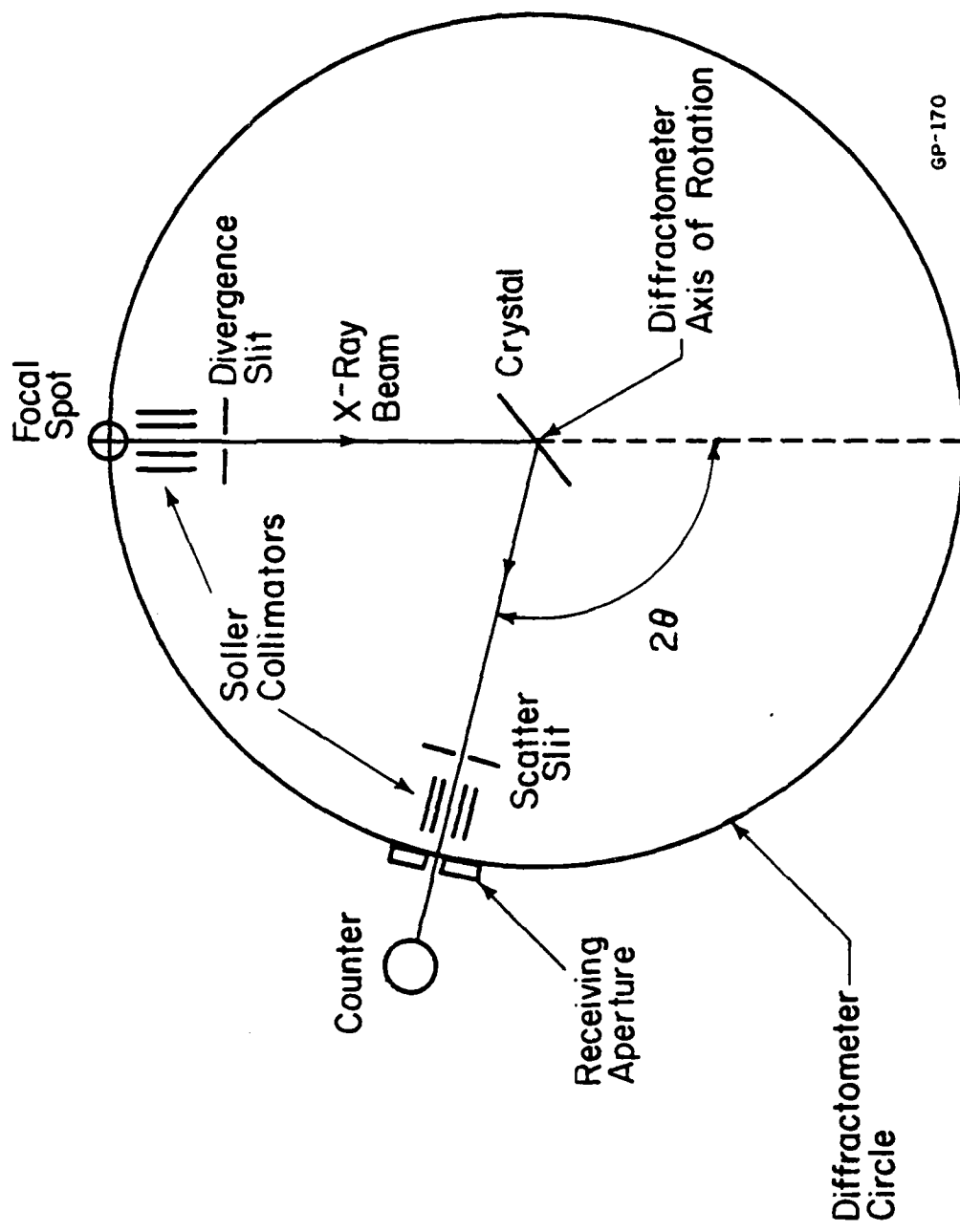


Figure 1. Plan view of the single crystal diffractometer used in this work.

axially divergent X-ray beams. The other collimators are vertical slits which limit the equatorial divergence of the X-ray beam.

The samples consist of an epitaxially grown InGaAsP layer on an InP substrate, with typical layer thicknesses from 2 to 15  $\mu\text{m}$ , while the substrate thickness is approximately 300  $\mu\text{m}$ . The samples are fixed to a stainless steel mount with a thin film of white wax (glycol phthalate). The mount fits into a spring-loaded fixture located at the diffractometer axis. Because the samples are slightly misoriented from the sawing and polishing procedures, they must be aligned before any diffraction can occur. The first step in the alignment procedure is to position and lock the detector at a strong reflection, usually (400), then manually rotate the crystal with the  $\omega$  drive until a strong signal is observed. The  $\omega$  setting is then locked, and then the  $2\theta$  position of the detector is changed to find the precise position of the  $\text{K}\alpha_1$  peak. Finally, the  $2\theta$  drive is locked while the  $\omega$  setting is readjusted to peak the signal.

#### E. X-ray Detection System

The X-ray detection system that records the X-ray intensity as the diffraction scan is made is shown in the block diagram of Fig. 2. The X-ray photons that pass through the receiving slit are detected by the proportional counter. The counter tube is filled with Xe gas at a pressure near one atmosphere and has a beryllium window which is virtually transparent to X-rays. The tube is biased at a voltage of 1840 V so that when an X-ray photon enters the tube and ionizes a Xe atom, the ionized electron acquires enough energy as it is accelerated to the anode of the tube to remove electrons from other atoms which, in turn, cause further ionization. Thus, there is a multiplication of over 1000 for each X-ray

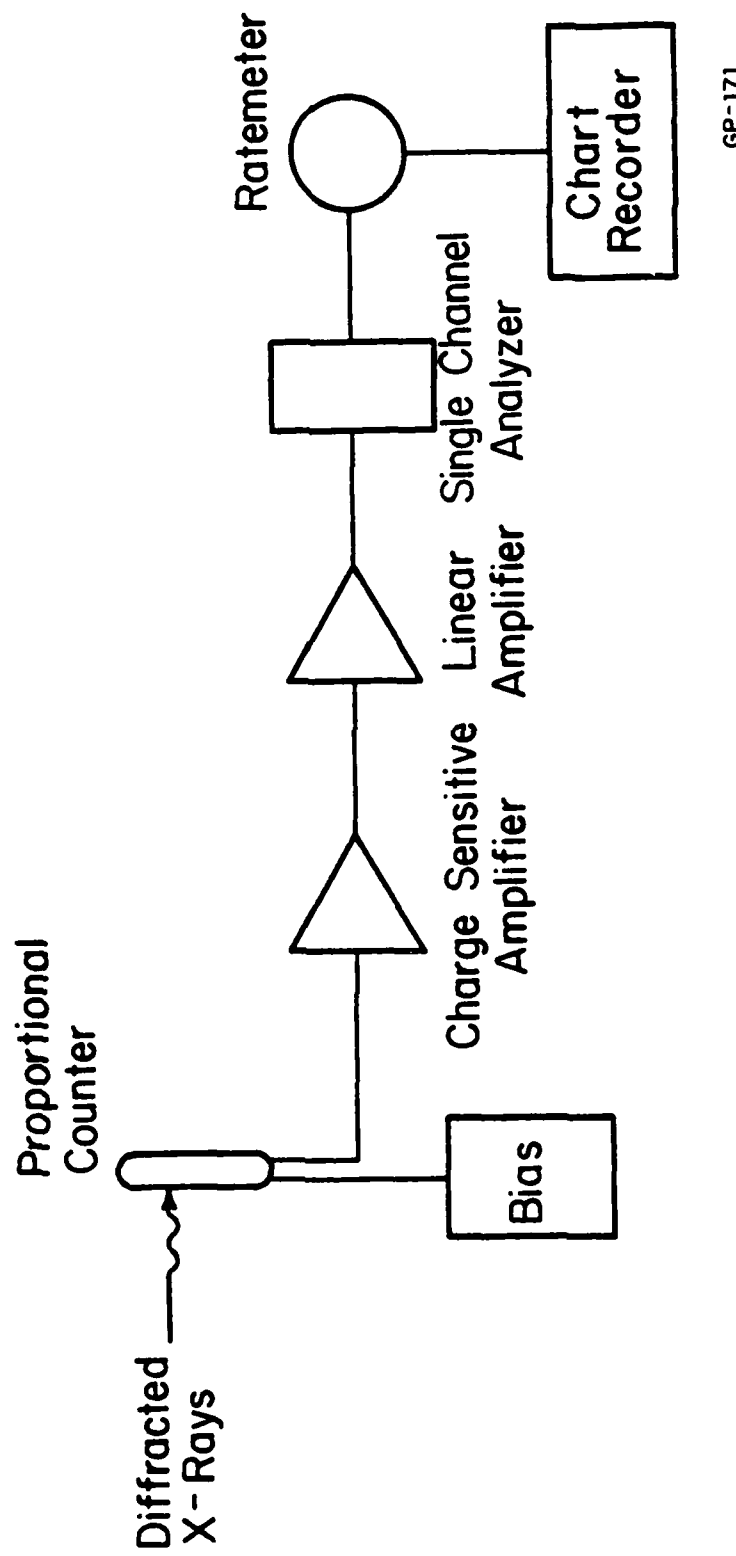


Figure 2. Block diagram of the X-ray detection system.

photon entering the tube. This detector is called a proportional counter because the tube generates an output pulse height which is proportional to the X-ray photon energy. The output pulse is amplified by the charge sensitive preamplifier and main amplifier to a level usable by the single channel analyzer (SCA).

The SCA generates a voltage pulse only when an incoming pulse is within the preselected voltage limits or equivalent energy range, thus increasing the signal-to-noise ratio by discriminating between the pulses of interest and those of higher and lower amplitudes. The output pulses from the SCA are converted to an analog rate (counts per second) by the ratemeter which is used to deflect the pen of the strip chart recorder to record the count rate (intensity) as a function of diffraction angle as the diffraction scan is made. It is crucial to optimize the SCA energy limits for a particular X-ray wavelength and main amplifier gain which determine the height of the pulses entering the SCA to obtain a good signal-to-noise ratio.

The voltage (energy) distribution of the pulses for the Cu  $K\alpha_1$  line is shown in Fig. 3 which is a plot of the ratemeter count rate as a function of the SCA E (Energy) setting (voltage). This plot was obtained by setting the diffractometer on the InP (400)  $K\alpha_1$  reflection and recording the count rate as the E setting was varied with a narrow  $\Delta E$  window setting of 0.1V. In order to maximize the signal intensity, the SCA acceptance window should include the main portion of the peak, and should reject voltage pulses above and below the peak to minimize extraneous signals. A good compromise is to place the boundaries of the acceptance window at approximately the 10% points of the distribution; in this case, the E setting would be 2.2 V with a  $\Delta E$  setting of 1 V which would result in the SCA generating a pulse

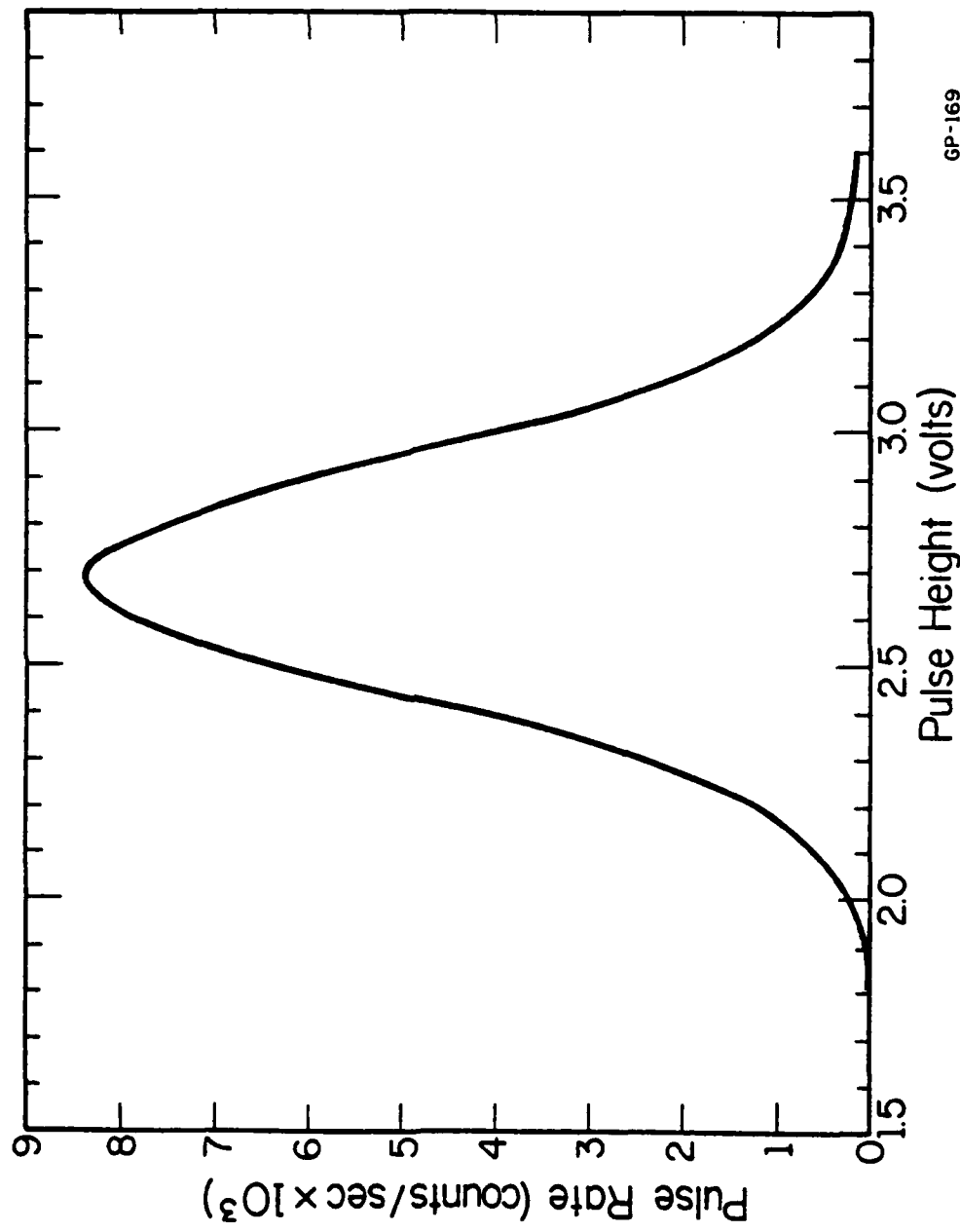


Figure 3. The count rate vs. SCA voltage with a 0.1 V  $\Delta E$  setting for the Cu  $K\alpha_1$  line.

only when an input pulse has an amplitude between 2.2 and 3.2 V. Although the SCA significantly improves the signal-to-noise ratio, it is incapable of resolving the  $K\alpha_1$  and  $K\alpha_2$  lines because they are spaced too closely in energy.

#### F. Typical Diffraction Curves

A set of three typical diffraction curves produced by the previously described diffractometer and X-ray detection system is shown in Fig. 4. The curves are the (600), (400), and (200) reflections from a polished (100)-InP substrate. Each reflection consists of a pair of diffraction peaks corresponding to the diffraction of the  $K\alpha_1$  and  $K\alpha_2$  lines produced by the Cu X-ray tube. The relative peak intensities between the three diffraction curves were made comparable by a change in the ratemeter range setting; the peak intensities actually decrease as the order of reflection increases. The  $K\alpha$  peaks of each reflection are distinguished by the fact that the  $K\alpha_1$  peak occurs at a lower angle than the  $K\alpha_2$  peak due to its slightly shorter wavelength with a peak intensity approximately twice that of the  $K\alpha_2$  peak.

Two general characteristics are apparent in Fig. 4 as a consequence of the property that the effective interplanar  $d$  spacing decreases as the reflection order increases causing the higher order reflection to occur at higher angles, and more importantly, increasing the angular separation or resolution between the  $K\alpha_1$  and  $K\alpha_2$  lines. When a lattice mismatched epitaxial layer is grown on the substrate, the diffraction of X-rays from the layer and substrate with different  $d$  spacings will cause two pairs of peaks to be observed, one  $K\alpha$  pair due to the layer and the other pair from the

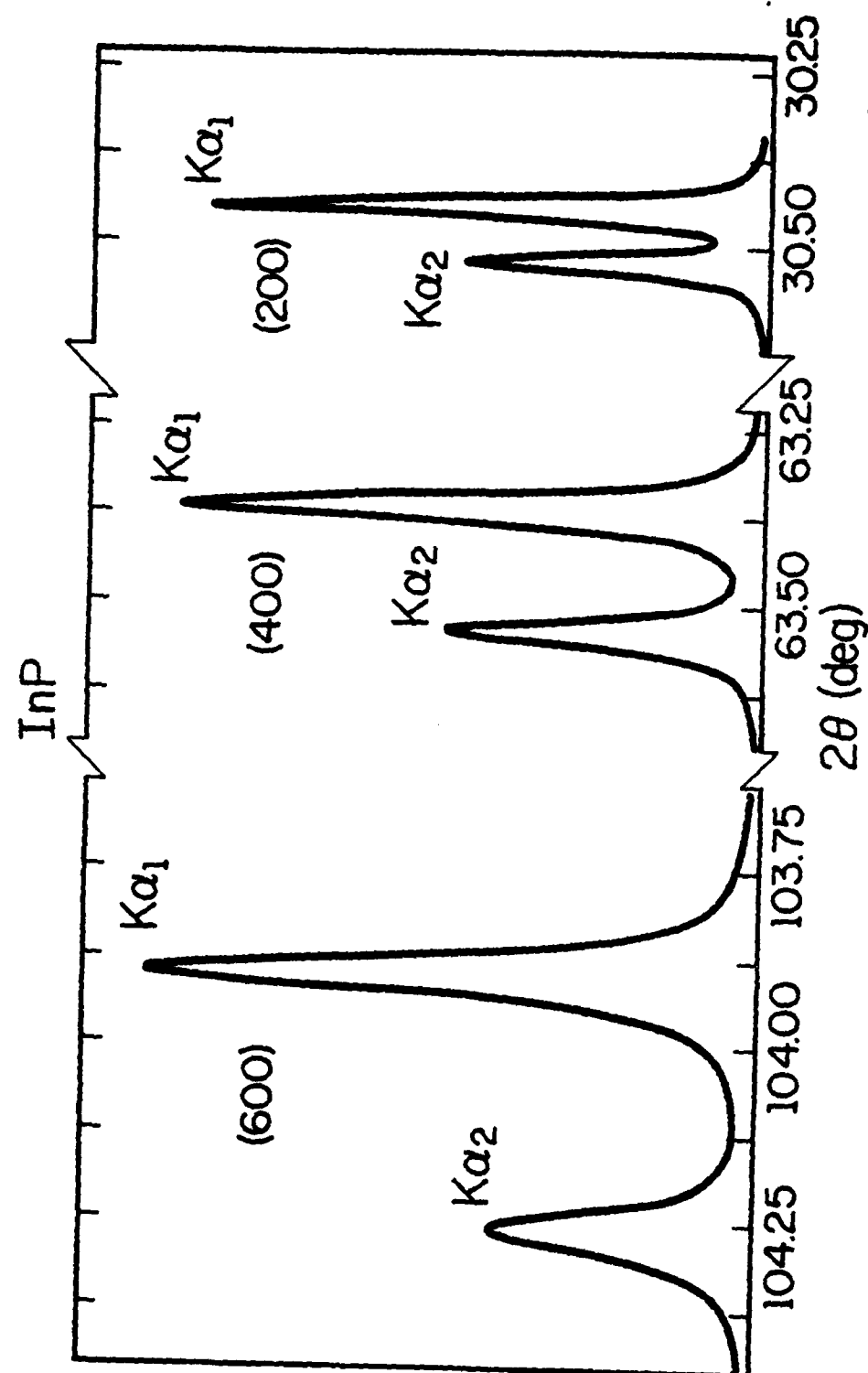


Figure 4. Typical intensity vs. Bragg angle diffraction curves for the (600), (400), and (200) reflections from a polished (100)-InP crystal.

GP-172

12

substrate. The amount of mismatch,  $\Delta a/a_{\text{InP}}$  ( $\Delta a = a_{\text{InGaAsP}} - a_{\text{InP}}$ ), is determined by the angular separations of the diffraction peaks, and as the reflection order increases, this separation will also increase because of the decrease in the  $d$  spacing which caused the increase in the separation between the  $K\alpha_1$  and  $K\alpha_2$  peaks in Fig. 4. Therefore, the highest possible reflection should be used to obtain the greatest resolution of the mismatch.

#### G. Absorption Effects

X-rays are absorbed by the atoms of the crystal and this effect is characterized by the linear absorption coefficient,  $\mu(\text{cm}^{-1})$ . The intensity,  $I(x)$ , of an X-ray beam after it has passed through a distance  $x$  of the material is given by the relation,  $I(x) = I_0 \exp(-\mu x)$ , where  $I_0$  is the intensity of the incident X-ray beam. The linear absorption coefficient is a constant for a particular crystal composition and X-ray wavelength and is on the order of  $1000 \text{ cm}^{-1}$  for the lattice matched InGaAsP/InP alloy family and Cu  $K\alpha$  radiation.

The effect of absorption is important because it can be used to identify the diffraction peaks of lattice mismatched layers by observing the behavior of the relative peak intensities at different reflections, since the path length  $x$  in the epitaxial layer is a function of the diffraction angle. As the reflection order ( $hkl$ ) decreases, the diffraction angle also decreases causing the X-ray beam to enter and exit at a more oblique angle, increasing the path length that the beam traverses in the epitaxial layer and reducing the intensity of the beam at the substrate. Therefore, the diffracted intensity from the substrate decreases relative to that from the layer as the order of the reflection decreases.

The absorption effect is enhanced by the phenomenon of secondary extinction, which is the reduction of the incident beam intensity as it

passes through the sample by the strong diffraction of X-rays from the material closest to the surface. Since secondary extinction is more pronounced at lower angles of diffraction,<sup>4</sup> the change in relative peak intensities from the layer and substrate with respect to the diffraction angle is due to both absorption and secondary extinction.

These effects are illustrated in Fig. 5 which shows diffraction curves for the (442) and (333) reflections of a mismatched ( $\Delta a/a = +0.1\%$ ) InGaAs epitaxial layer grown on a (111)-InP substrate. At the higher (442) reflection, the peak from the substrate is much stronger than that of the layer with the ratio of intensities being  $I_L/I_S = 0.38$ , where  $I_L$  and  $I_S$  refer to the peak heights of the layer and substrate respectively. At the lower (333) reflection, which occurs at a lower angle, the peak from the layer is now stronger than that of the substrate, with the ratio of  $I_L/I_S = 1.32$ . The behavior of the relative peak intensities is in complete accord with effects of absorption and secondary extinction.

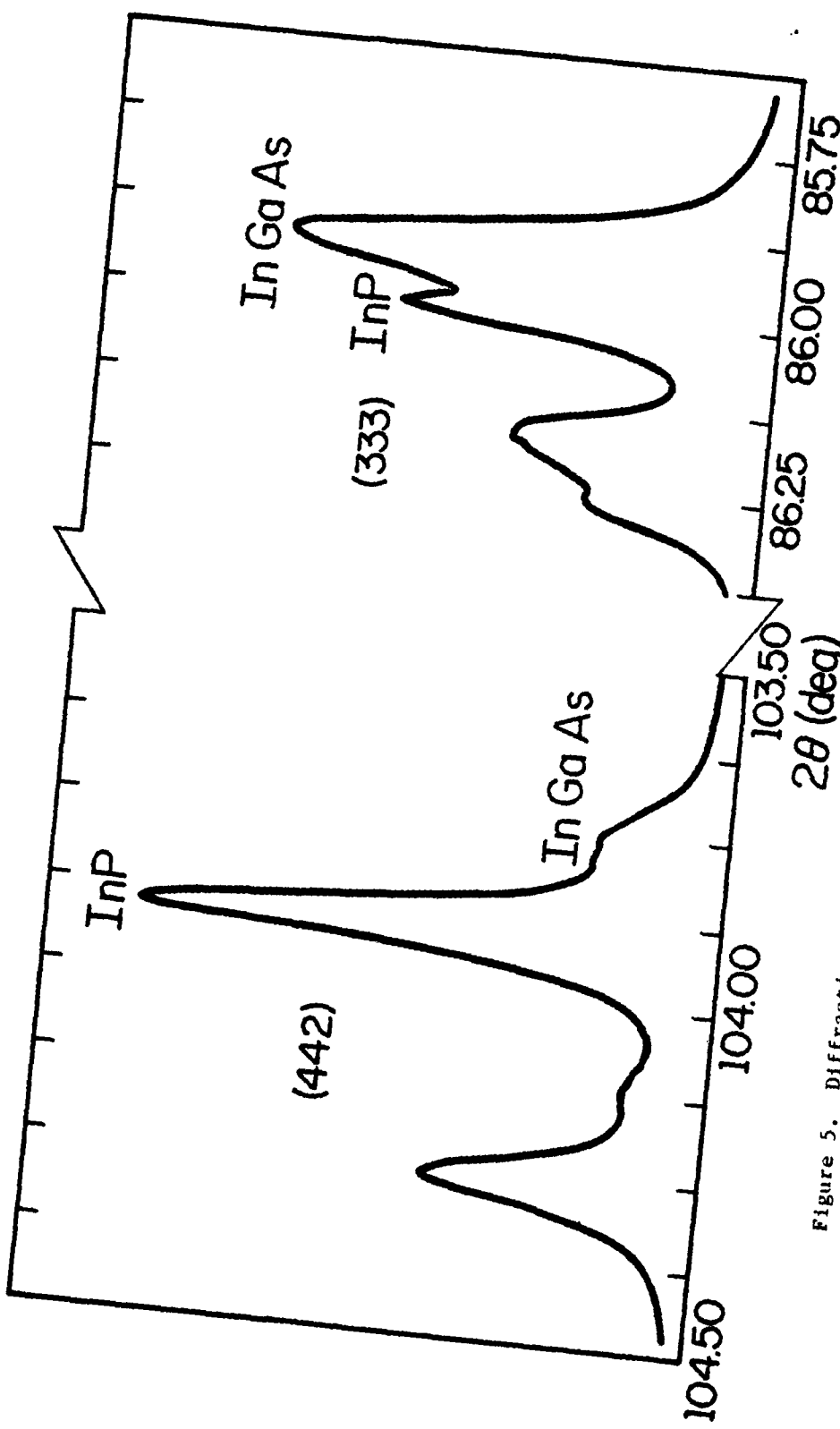


Figure 5. Diffraction curves for the (442) and (333) reflections from the InGaAs layer which is lattice mismatched to the (111)-InP substrate showing the effects of absorption and secondary extinction.

## III. EXPERIMENTAL RESULTS - LPE GROWTH

A. Crystal Growth

The epitaxial layers used in this work were grown by liquid phase epitaxy (LPE) on (100) oriented InP substrates polished with a 1% bromine-methanol solution. The growth system consisted of a multiple-well horizontal slider boat constructed of high purity graphite enclosed in a quartz tube. A hydrogen gas ambient within the tube was produced by a Pd purifier. The heating element was enclosed by a semitransparent liner coated with a gold film and mounted on rails so it could be slid over the furnace tube. This particular growth furnace offers the advantages of rapidly heating and cooling the slider boat and visually determining the liquidus temperature of the growth melts. The growth melts were composed of accurately weighed amounts of GaAs, InAs, InP (for the quaternary layers), and dopant for the doped layers, added to 1.2 g of In to form melts saturated at 650°C for the quaternary and 630°C for the ternary.

The various temperature-time growth programs used in this work are shown in Fig. 6. Although the times and temperatures in Fig. 6 are only applicable to the growth of the quaternary, the terminology for the various growth techniques that is discussed later applies equally well to the ternary growths which were done at lower temperatures. Three different LPE growth techniques are shown, step-cooling, super-cooling, and equilibrium-cooling. Prior to growth, all three techniques follow the same heating procedure, the furnace tube is purged at room temperature after loading

## TIME - TEMPERATURE PROFILE FOR GROWTH

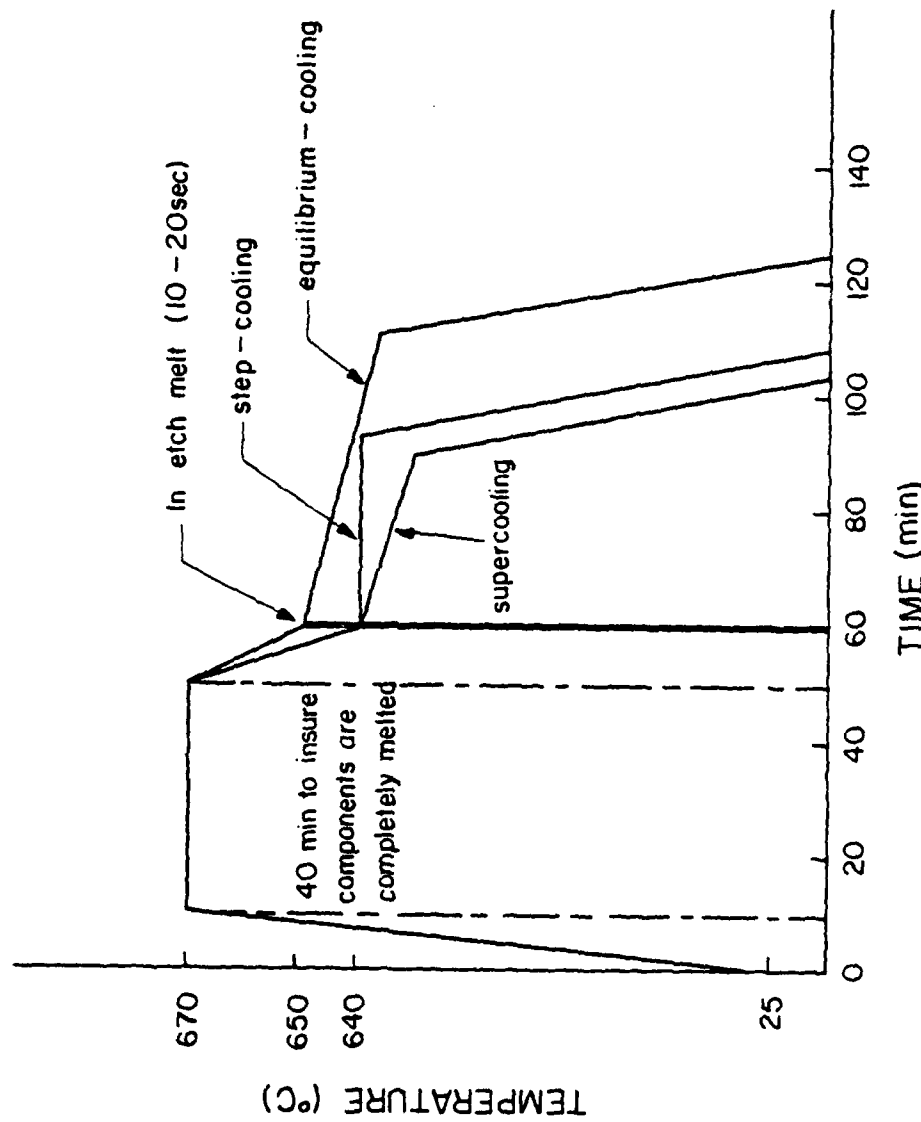


Figure 6. Temperature-time growth programs used in this work.

the substrate with hydrogen gas for 30 or more minutes to flush air and water vapor out of the system. After purging, the furnace is moved over the tube to rapidly heat the system to approximately 670°C and held at this temperature for a minimum of 40 min. to ensure that the melt constituents are completely dissolved. During this period, the substrate becomes thermally damaged due to the phosphorous loss from the surface. After the temperature is reduced to the initial growth temperature, the substrate is slid under a well containing pure In to etch the surface and eliminate the thermally damaged portion of the substrate. Growth is initiated by sliding the substrate under the growth melt and terminated by sliding the substrate out into an empty well. The furnace is then slid off the tube to allow for rapid cooling to room temperature. The three growth techniques are characterized by the method in which the temperature varies with time during growth. For step-cooling, the growth temperature,  $T_G$ , is held at a constant value of supersaturation,  $\Delta T$ , during growth, while for super-cooling, the temperature is decreased linearly (ramped) after an initial supersaturation during growth. In the case of equilibrium cooling, no supersaturation is used and the growth run starts at the saturation temperature and the temperature is ramped down from there until the termination of growth.

After growth, the lattice mismatch was determined by X-ray diffraction and the band gap of the layers was determined by optical spectrophotometer transmission measurements of the sample with the substrate side polished to reduce scattering. The wavelength corresponding to the bandgap,  $\lambda_g$ , was identified with the wavelength at the 50% point between the maximum and minimum values of transmission.

The lattice mismatch is defined as  $\Delta a/a_{\text{InP}}$  where  $\Delta a = a_{\text{InGaAsP}} - a_{\text{InP}}$ , and thus a positive mismatch means the lattice constant of the layer is greater than that of the substrate. Since a symmetric diffraction geometry was used, the lattice mismatch measured is the component perpendicular to the (100) surface and includes any strain in the (100) direction induced in the quaternary layer.<sup>5,6</sup> The diffraction peak from the substrate serves as an internal standard for the InP lattice constant as well as offering a qualitative measure of the crystal quality and compositional uniformity of the grown layer by comparison of the diffraction line widths. In addition, the diffracted intensities from the layers and the substrate were comparable and made the measurement of line positions convenient. The thicknesses of the epitaxial layers for the samples studied ranged from 2  $\mu\text{m}$  to 15  $\mu\text{m}$ . The half maximum peak widths for material with a uniform lattice parameter were about 220 s of arc, while peak widths for graded composition material were significantly broader. The minimum amount of lattice mismatch resolvable for these conditions was approximately 0.02%.

#### B. Determination of Distribution Coefficients

In the LPE growth of the InGaAsP alloy on InP, it is of fundamental importance to understand the interrelationship between the composition of the growth melt and the composition of the resultant epitaxial layer for a specific set of growth conditions. This relationship is expressed in terms of the distribution coefficient,  $K_i$ , which is defined as the ratio between the atomic fraction of the alloy component  $i$  in the solid and the atomic fraction of this component in the In melt,  $K_i = X_i^s/X_i^l$ .

The experimentally determined distribution coefficients for the growth of closely lattice matched InGaAsP in the spectral region between 1.15 and 1.31  $\mu\text{m}$  is shown in Fig. 7. These data have been presented in tabular

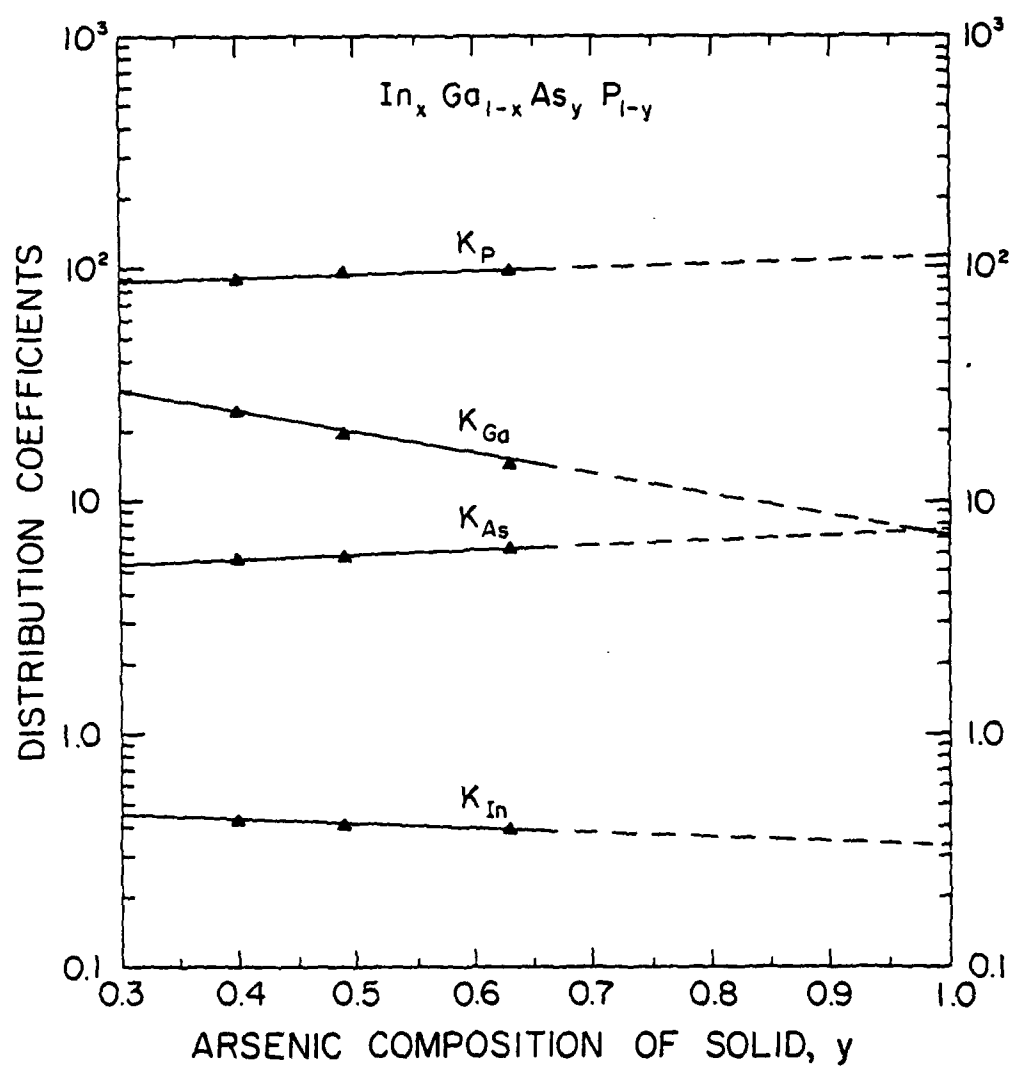


Figure 7. Distribution coefficients as a function of  $y$ , the As composition of the grown layer.

form elsewhere to facilitate a more accurate determination of the melt composition.<sup>7</sup> The epitaxial layers were grown by the step-cooling technique at 640°C from undoped melts which were saturated at 650°C. The distribution coefficients of the four melt constituents are plotted as a function of  $y$ , the As composition of the  $In_xGa_{1-x}As_yP_{1-y}$  solid. The three data points are the solid compositions, as determined by electron microprobe measurements, corresponding to band gap wavelengths of 1.15, 1.21, and 1.31  $\mu\text{m}$  for increasing  $y$ . The compositional dependence of the distribution coefficients, especially the large decrease in  $K_{\text{Ga}}$  with  $y$  in this spectral region, makes a trial-and-error determination of the proper melt composition for lattice matched growth difficult. However, once the correct melt composition is determined, lattice matched epitaxial layers with the desired band-gap energy can be grown reproducibly. In order for these distribution coefficients to be meaningful, the closeness to lattice match of the grown layers must be verified, and is demonstrated by the (600) diffraction curves in Fig. 8 for four different samples spanning the 1.15 to 1.31  $\mu\text{m}$  range. Curve (a) on the left- and right-hand portions of Fig. 8 is from a (100) InP crystal and is shown for reference purposes. Curves (b) and (c) are for 1.15 and 1.31  $\mu\text{m}$  material, respectively, and exhibit a close lattice match with  $\Delta a/a < \pm 0.03\%$ , the resolution limit for this particular measurement. Curve (d) is for a  $\lambda_g = 1.21 \mu\text{m}$  layer, and although a small amount of mismatch is observed ( $\Delta a/a = +0.05\%$ ), the data obtained from this growth run were used for the  $y = 0.49$  distribution coefficient point in Fig. 7. Curve (e) is for a  $\lambda_g = 1.31 \mu\text{m}$  layer with a solid composition identical to the sample in curve (c) as determined by the electron microprobe measurement yet exhibits a mismatch of +0.06% which indicates the extreme sensitivity

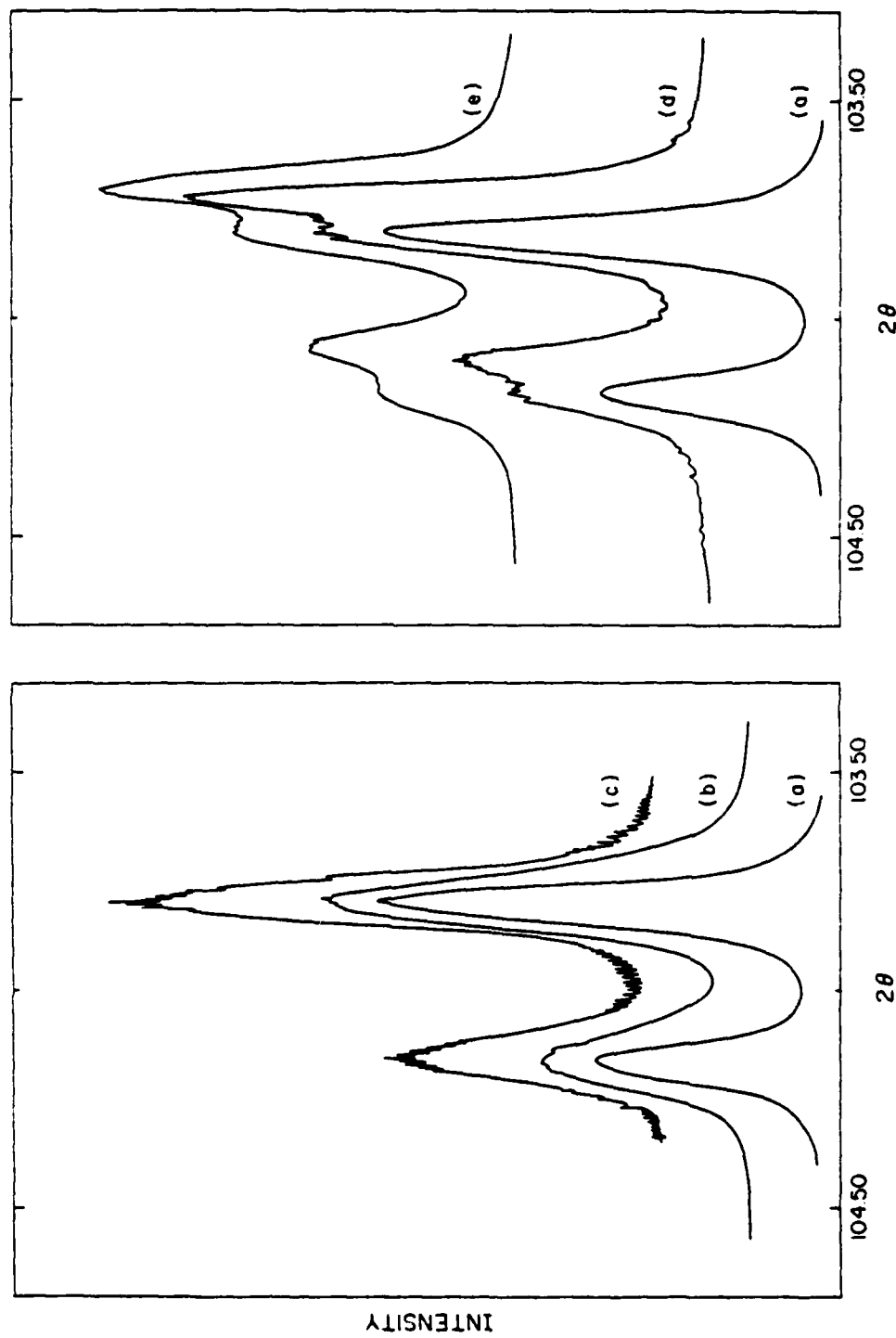


Figure 8. (600) diffraction curves for layers of various solid compositions.

of the X-ray diffraction technique for determining the lattice matched condition.

#### C. Effects of Lattice Mismatch on Surface Morphology

A practical consideration that must be taken into account if these InGaAsP layers are to be used for the fabrication of useful devices is the surface morphology and crystallographic quality of these layers. It has been demonstrated that there is a compositional (energy gap) dependence of the influence of lattice mismatch on the surface morphology and misfit dislocation density of LPE InGaAsP layers.<sup>8</sup> Larger band-gap quaternary layers ( $\lambda_g \leq 1.21 \mu\text{m}$ ) can tolerate relatively high amounts of lattice mismatch ( $\Delta a/a \approx 0.2\%$ ) and still have a specular surface with no visible misfit dislocations. This is not the case for larger  $\lambda_g$  compositions, since even with  $\Delta a/a = +0.05\%$  for  $1.31 \mu\text{m}$  material, these layers have a rough surface morphology with misfit dislocations observed in the cleaved cross section of the layer. A similar behavior is observed for InGaAs,  $\lambda_g = 1.68 \mu\text{m}$ . Thus, it is important to maintain a close lattice match ( $\Delta a/a < 0.03\%$ ) in order to have a high quality surface suitable for device fabrication for the larger wavelength ( $\lambda_g > 1.21 \mu\text{m}$ ) quaternary composition.

#### D. Variation of Melt Composition

A topic related to the determination of the distribution coefficients is the behavior of the lattice mismatch and bandgap of the epitaxial layer as the melt composition is varied about the one composition that yields a lattice matched layer of the desired band gap at a particular growth temperature. This study was performed in detail for the lattice matched unintentionally doped quaternary with a band gap wavelength of  $1.15 \mu\text{m}$  grown by step-cooling at  $640^\circ\text{C}$ .<sup>9</sup>

Figure 9 illustrates the effect of the variation of the atomic fraction of As in the melt,  $X_{\text{As}}^l$ , on the diffraction curves of four samples with  $X_{\text{As}}^l$  increasing from curves (a) to (d). The lattice mismatch is indicated by the separation between the  $\text{K}\alpha$  doublet of the layer, denoted  $\text{QK}\alpha_1$  and  $\text{QK}\alpha_2$ , and the  $\text{K}\alpha$  doublet of the InP substrate,  $\text{InP K}\alpha_1$  and  $\text{InP K}\alpha_2$ . Curve (b) is for a melt of the proper composition to produce the lattice matched condition where the  $\text{K}\alpha$  doublets of the layer and substrate are superimposed. The diffraction peak profiles from the layers are as sharp as those from the substrate and indicate layers of good crystal quality and uniform composition.

The information in Fig. 9 along with data from additional samples are summarized by the plot of lattice mismatch versus  $X_{\text{As}}^l$  in Fig. 10. As  $X_{\text{As}}^l$  is increased from 3.35% to 3.93%, the mismatch varies linearly from -0.15% to +0.32%. Over this same range of  $X_{\text{As}}^l$ , the bandgap wavelength,  $\lambda_g$ , increases from 1.125  $\mu\text{m}$  to 1.216  $\mu\text{m}$ .

A similar investigation was performed to determine the effects of the variations of the Ga and P atomic fractions in the growth solution. Figure 11 shows that both the lattice mismatch and bandgap wavelength decrease with increasing  $X_{\text{Ga}}^l$ , with the influence on the mismatch being greater than the effect on  $\lambda_g$ . The lattice mismatch decreases linearly from +0.24% to -0.13% and  $\lambda_g$  changes slightly from 1.162  $\mu\text{m}$  to 1.152  $\mu\text{m}$  as  $X_{\text{Ga}}^l$  increases from 0.34% to 0.44%. The variation of  $X_{\text{P}}^l$  causes very little change in either the lattice mismatch or  $\lambda_g$  as shown in Fig. 12. However, as the atomic fraction of P is increased above about 0.40%, nucleation in the melt occurs before the growth temperature of 640°C is attained, and the two-phase solution growth results in a lattice mismatched layer.

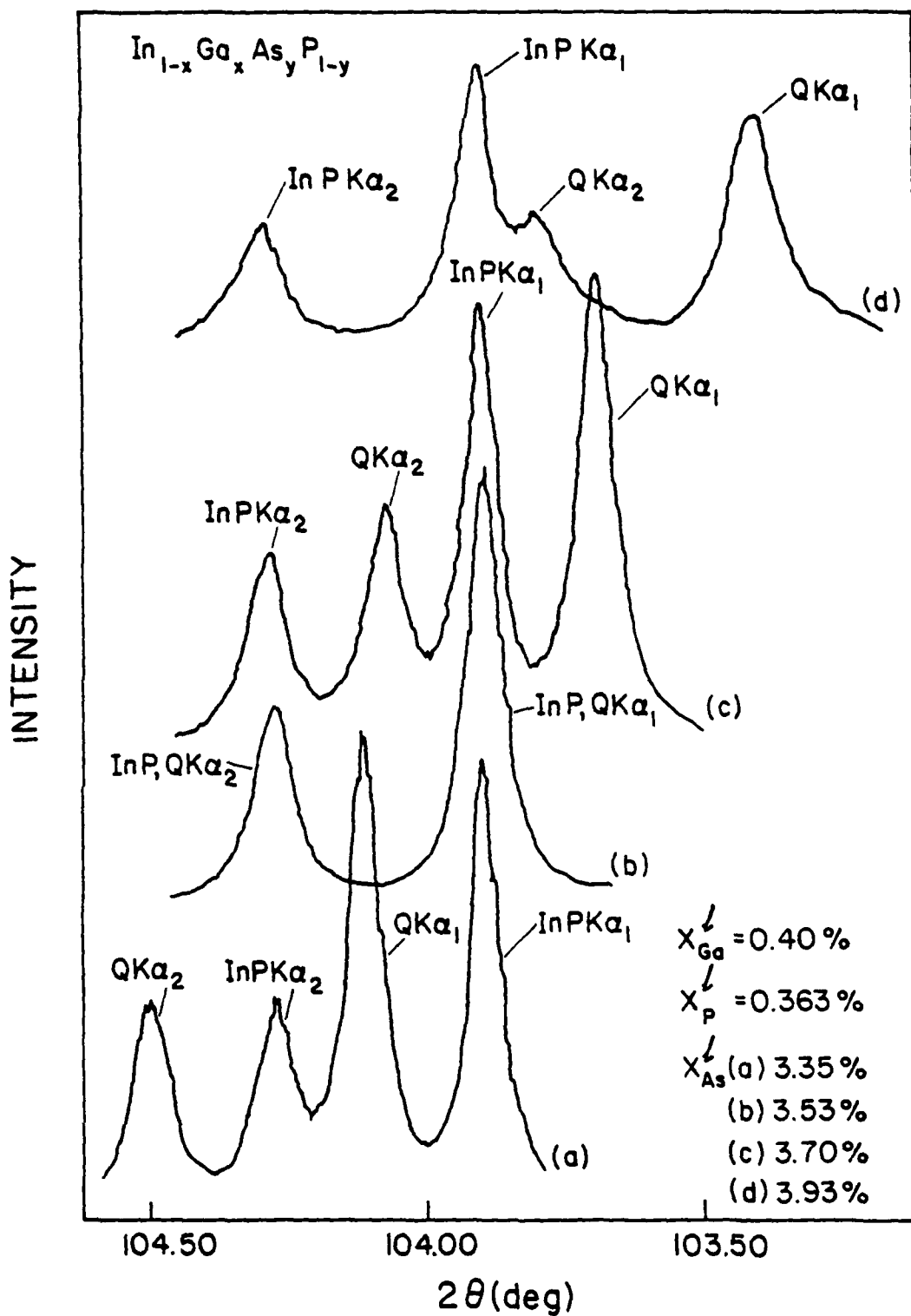


Figure 9. (600) diffraction curves for four samples grown from melts with differing amounts of As.

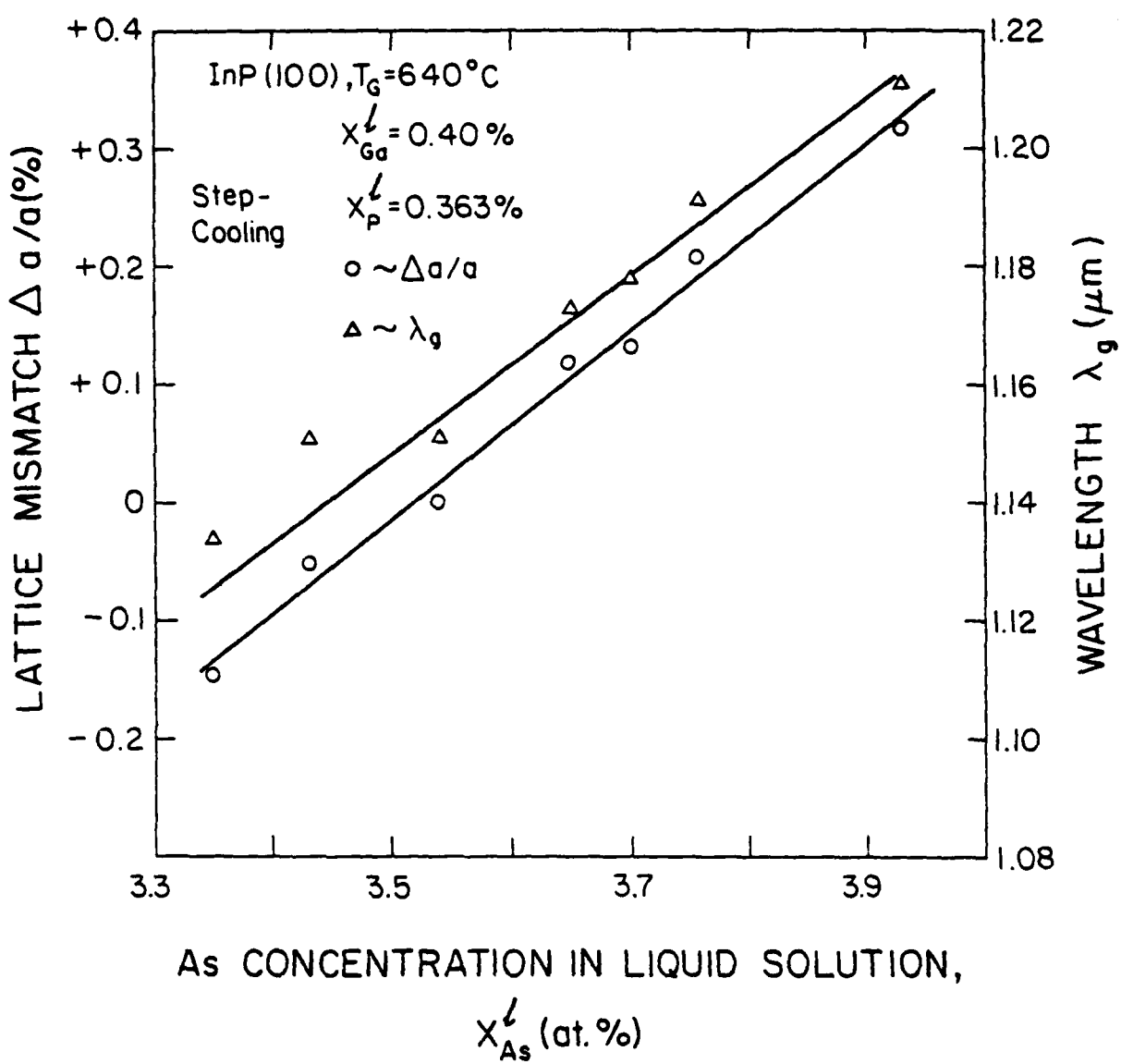


Figure 10. The variation of lattice mismatch and bandgap wavelength with the atomic fraction of As in the melt.

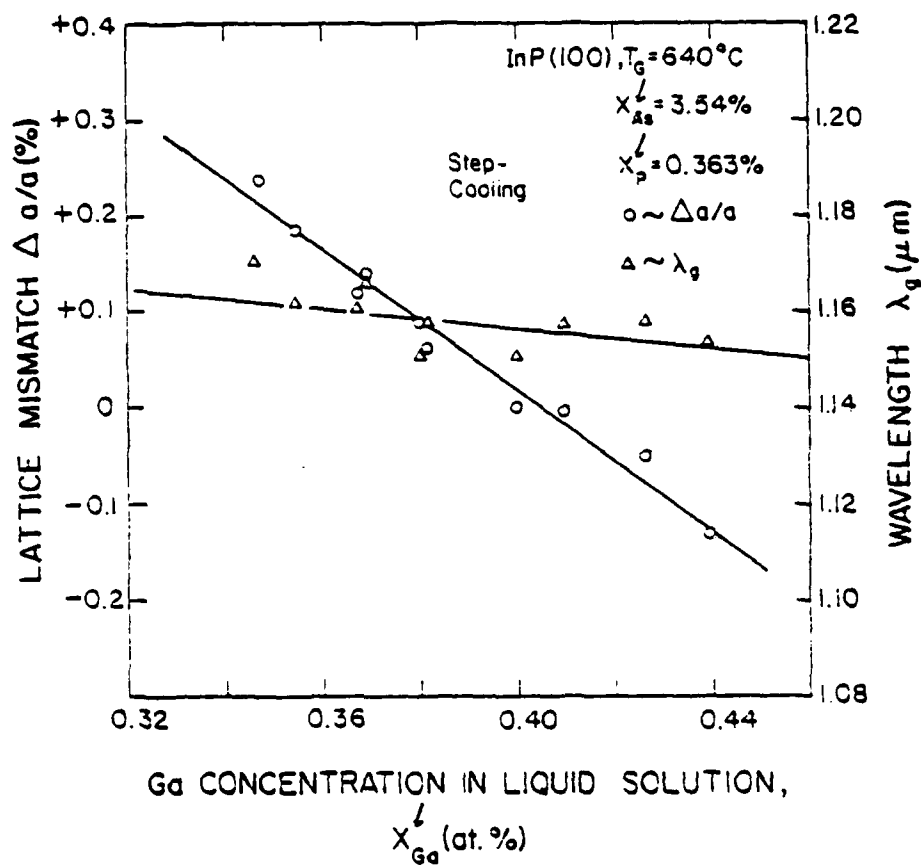


Figure 11. The variation of lattice mismatch and bandgap wavelength with the atomic fraction of Ga in the melt.

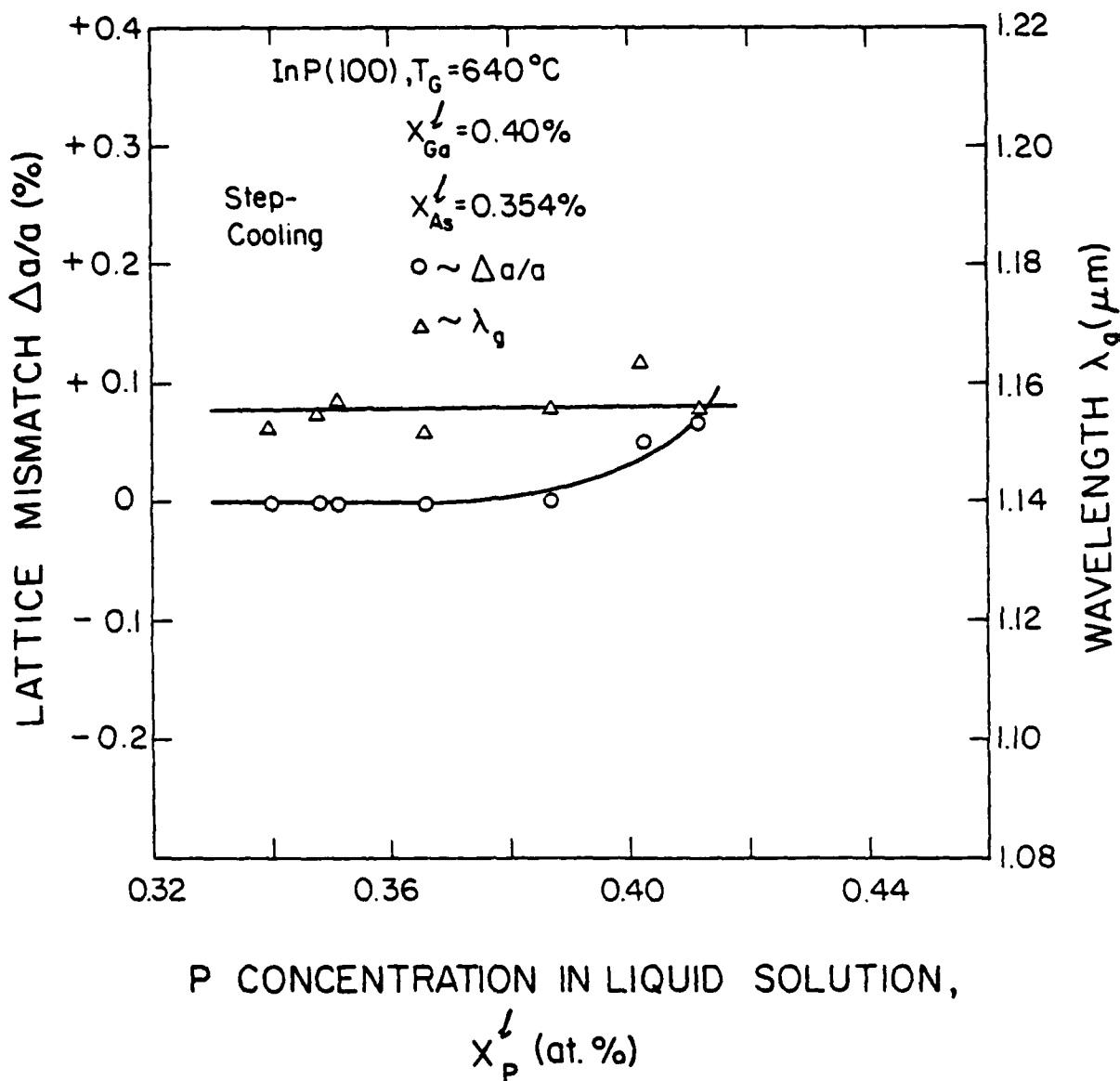


Figure 12. The variation of lattice mismatch and bandgap wavelength with the atomic fraction of P in the melt.

Thus, large changes in the lattice constant of the epitaxial layer can be accomplished by varying either  $X_{\text{As}}^{\lambda}$  or  $X_{\text{Ga}}^{\lambda}$  while a great variation in  $\lambda_g$  can be obtained by altering  $X_{\text{As}}^{\lambda}$ .

#### E. Effect of Growth Temperature

Lattice mismatch also results when the melt composition is maintained constant and a growth temperature different from the one that produces a lattice matched layer is used.<sup>9,10</sup> This is illustrated in Fig. 13 which displays diffraction curves for layers grown at three different temperatures from melts of identical composition. Curve (b) indicates lattice match when  $T_G = 640^{\circ}\text{C}$ , while curve (a) shows positive mismatch of +0.12% for  $T_G = 635^{\circ}\text{C}$  and curve (c) shows negative mismatch of -0.10 for  $T_G = 645^{\circ}\text{C}$ . Although the curves in Fig. 13 show considerable lattice mismatch, the line widths of the layer diffraction peaks are comparable to the InP line widths indicating that the layers are of uniform composition and good crystal quality.

The dependences of mismatch and  $\lambda_g$  on growth temperature are plotted in Fig. 14. Both parameters decrease significantly as the growth temperature approaches the saturation temperature, i.e., as the super saturation temperature decreases. Figure 14 indicates that growth with a nonconstant temperature-time program in this temperature range will result in a layer with varying mismatch and  $\lambda_g$ , i.e., a compositionally graded layer.

Evidence of this effect can be seen in both the single crystal and double crystal diffraction rocking curves in Fig. 15, which compare a layer grown by step cooling with one grown with super cooling. Curves (a) and (c) correspond to a 5  $\mu\text{m}$  quaternary layer grown by step cooling. The double crystal measurement (c), which resolves only the  $\text{K}\alpha_1$  line, shows that the InGaAsP layer produces a sharp peak of comparable width to that

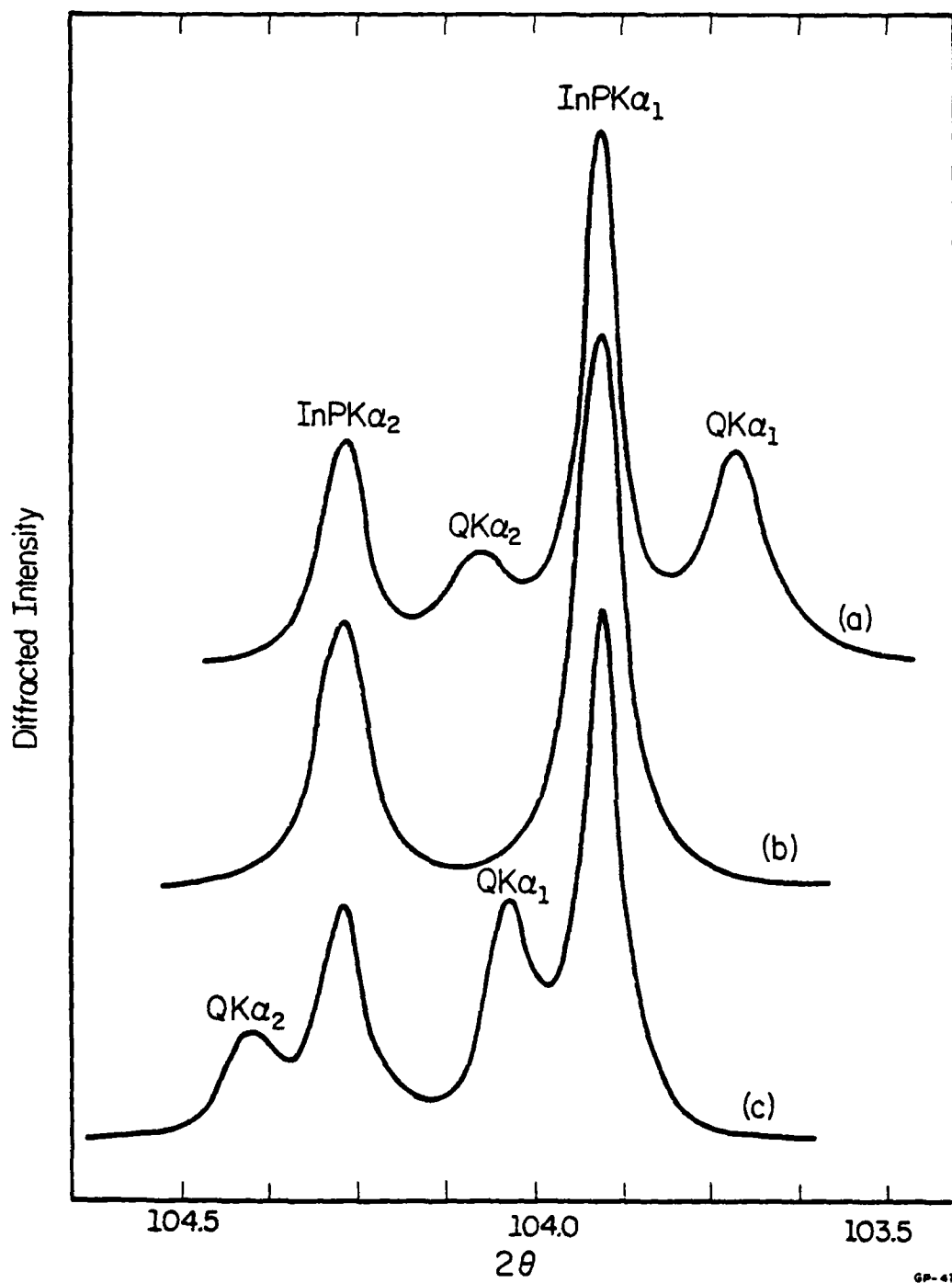


Figure 13. (600) diffraction curves for three quaternary layers grown at three different temperatures: (a)  $635^{\circ}C$ , (b)  $640^{\circ}C$ , and (c)  $645^{\circ}C$ .

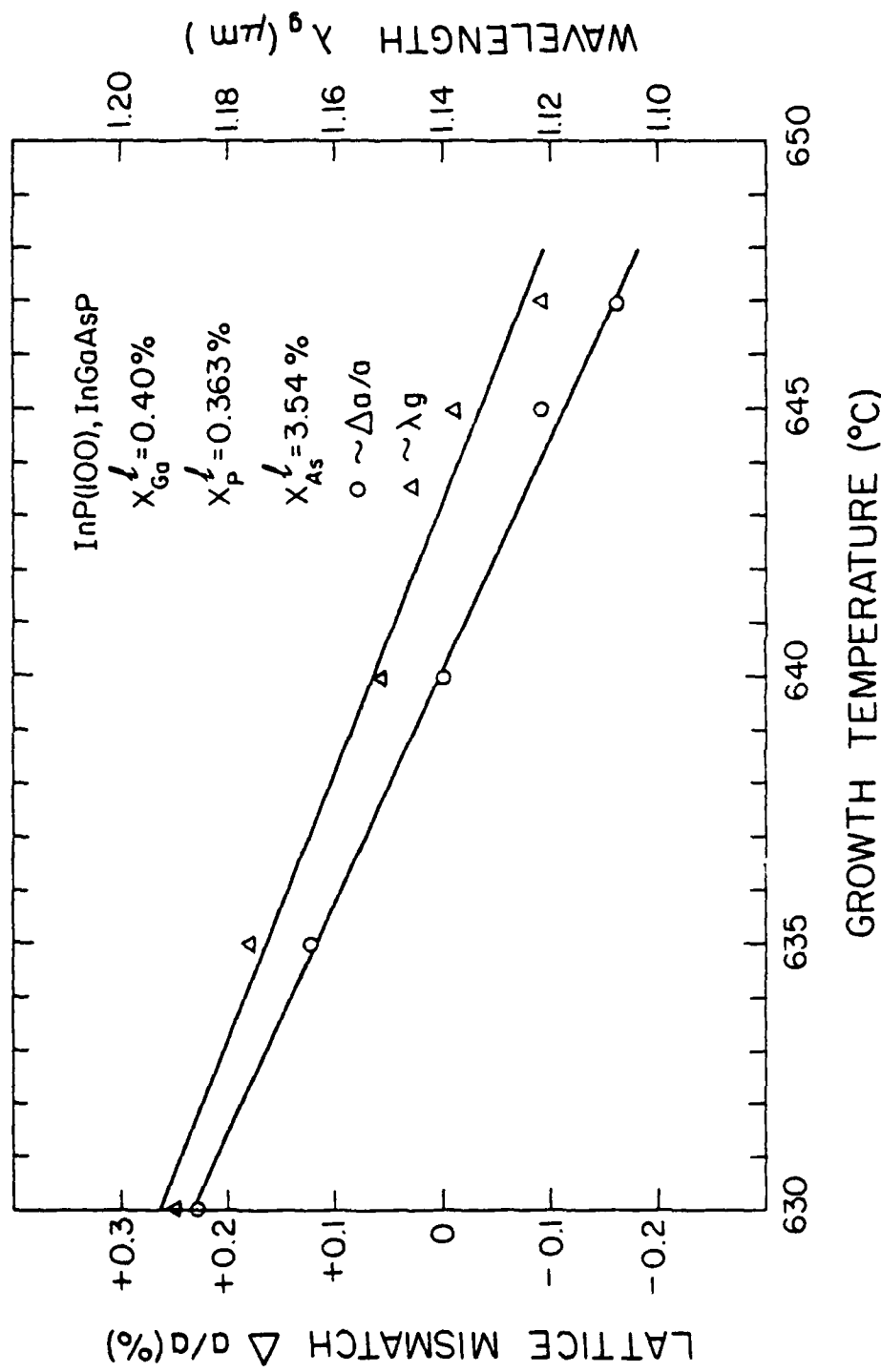


Figure 14. The variation of lattice mismatch and bandgap wavelength with the growth temperature for the step cooling growth technique.

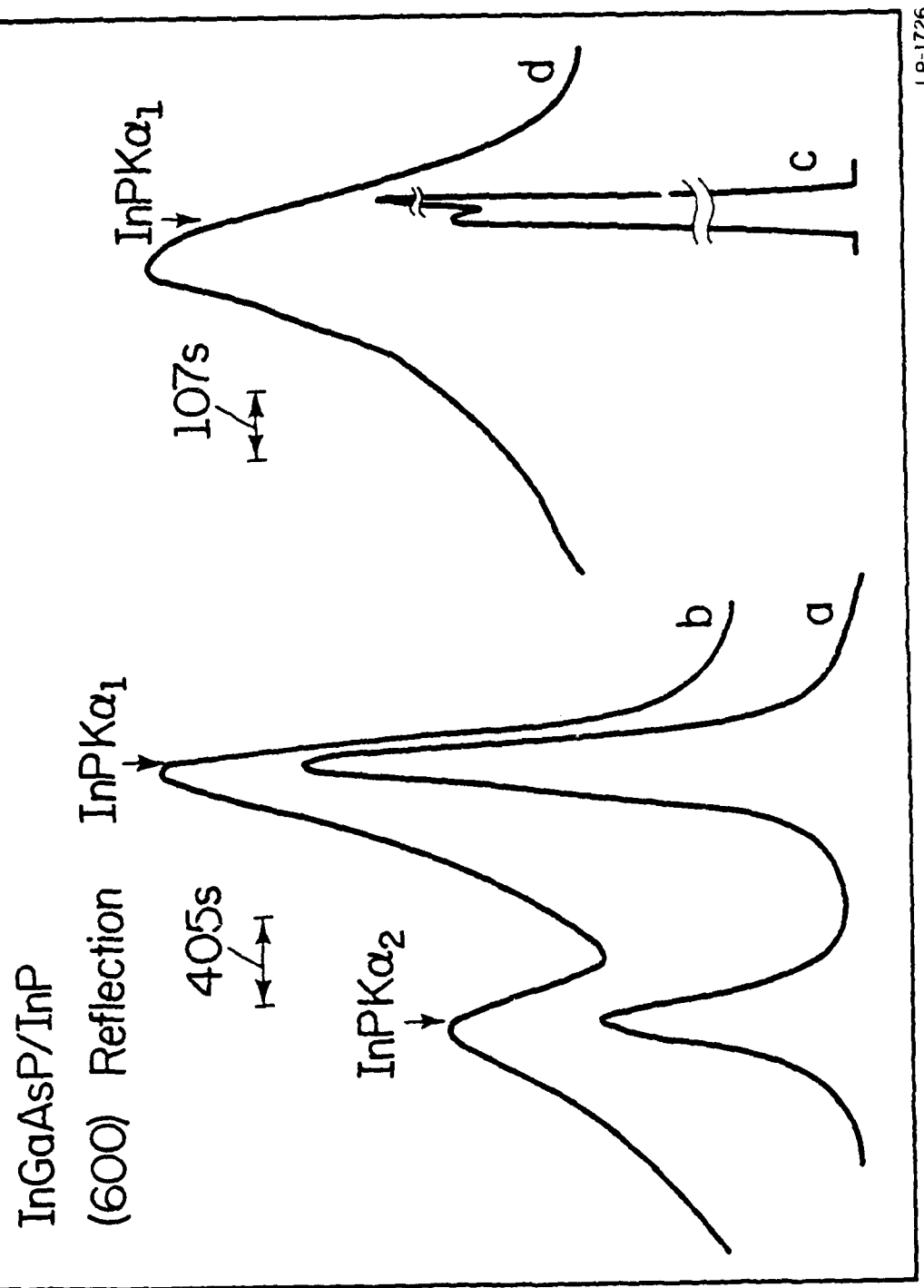


Figure 1. (600) single and double crystal diffraction curves for a step cooled and a super cooled sample. Curves (a) and (c) are for the step cooled sample measured with single and double crystal diffractometer, respectively. Curves (b) and (d) are for the super cooled sample measured with a single and double crystal diffractometer, respectively.

of the InP substrate with an indicated lattice mismatch of +0.006% that cannot be resolved in the single crystal measurement (a). The narrow width of the quaternary peak in (c) indicates that the layer is compositionally uniform. Curves (b) and (d) for a super cooled sample ( $\Delta T = 3^\circ\text{C}$ ,  $R = 0.3^\circ\text{C}/\text{min}$ , and a total growth time of 33 min) show that the 8  $\mu\text{m}$  thick layer is compositionally nonuniform due to the changing growth temperature as indicated by the marked broadening of both the single (b) and double crystal (d) diffraction peaks from the layer.

#### F. Effect of Growth Technique

##### 1. Super cooling

Additional studies were conducted on  $\lambda_g = 1.15 \mu\text{m}$  quaternary layers grown by the super cooling technique with  $\Delta T = 10^\circ\text{C}$  and cooling rates of 0, 0.25, 0.40, 0.80, and  $1.0^\circ\text{C}/\text{min}$  for a growth period of 10 min.<sup>11</sup> The diffraction curves of four of the five samples with  $R$  increasing from 0 to  $0.80^\circ\text{C}/\text{min}$  from curves (1) to (4) are shown in Fig. 16. Curve (1) is for  $R = 0^\circ\text{C}/\text{min}$ , i.e., growth by step cooling and the layer is lattice matched to the substrate as indicated by the superposition of the InP and quaternary  $\text{K}\alpha_1$  and  $\text{K}\alpha_2$  diffraction peaks. As  $R$  increases, the range of temperature during the growth period increases, causing compositional grading of the layer. The variation of mismatch with  $T_G$  in Fig. 14 shows that, as the growth temperature is reduced, the lattice mismatch increases positively which is exactly the behavior shown in curves (2)-(4) in Fig. 16. As the cooling rate increases, the diffraction peaks become broader and the leading edge shifts to more positive values of mismatch. The broad structureless quaternary single crystal diffraction peaks seem to indicate that the lattice mismatch varies continuously during growth, however, it has been

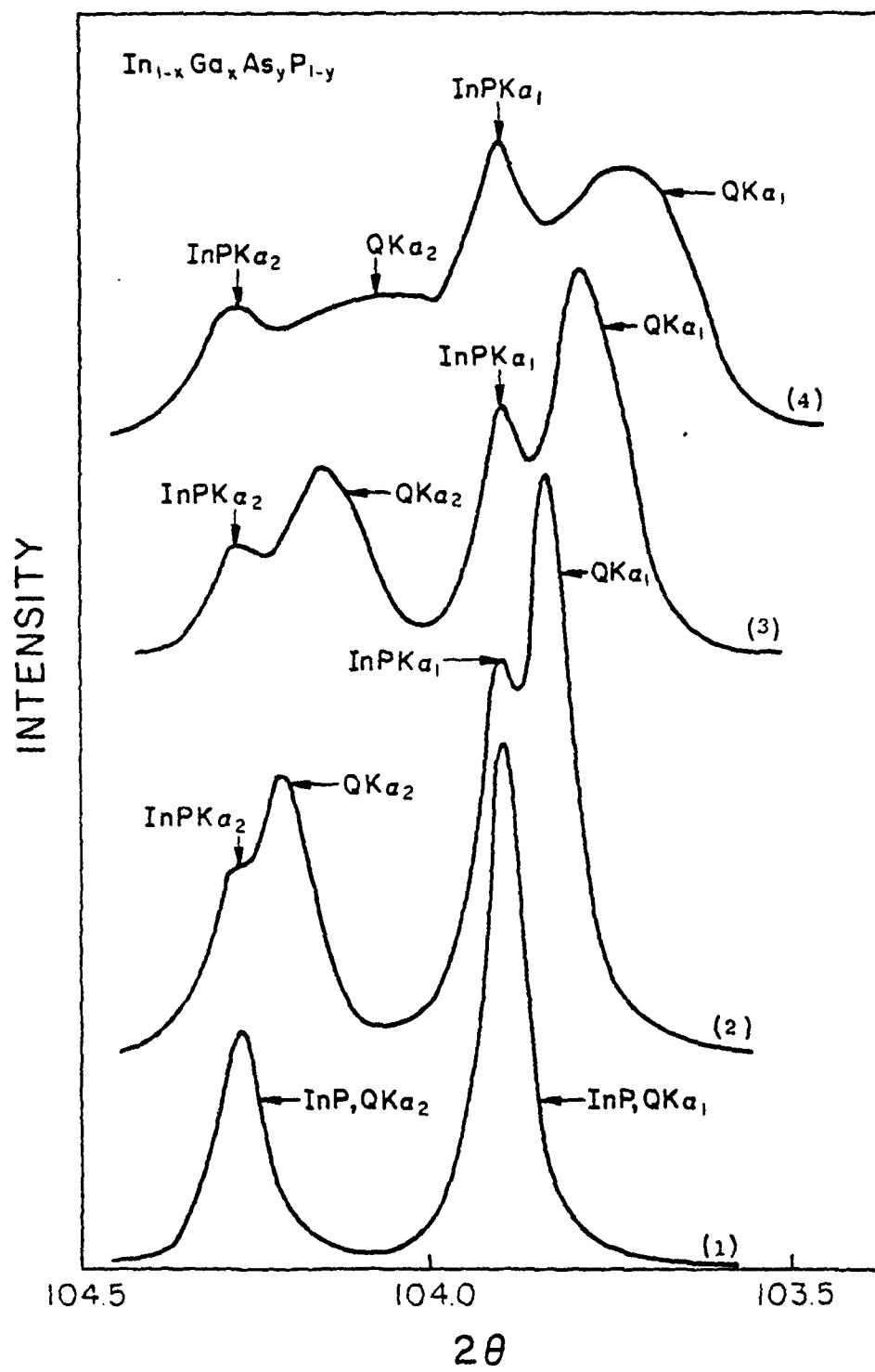


Figure 16. (600) diffraction curves for samples grown with an initial supersaturation of 10°C and cooling rates  $R$  of (1) 0, (2) 0.25, (3) 0.40, and (4) 0.80°C/min.

reported recently that a stepwise variation in mismatch was observed, with several discrete diffraction peaks from the layer, using a double crystal diffractometer to measure super-cooled samples.<sup>12</sup>

## 2. Equilibrium cooling

Compositional grading is also observed when the equilibrium cooling growth technique, where the cooling rate is used with no supersaturation, is utilized. An example is shown in Fig. 17 where curve (a) is the profile for a layer grown with  $R = 1.2^\circ\text{C}/\text{min}$  over the temperature range  $650^\circ\text{C}$  to  $639^\circ\text{C}$  and indicates a small positive mismatch. The layer thickness was approximately 4  $\mu\text{m}$ .

This sample was then etched in a 0.5% Br-methanol solution with part of the sample masked so that the amount of material removed could be measured with a surface profilometer. The X-ray measurement was repeated with the unetched portion of the sample shielded by lead foil to insure that only the etched part of the sample was measured. This procedure was repeated, producing the series of curves (b) to (d), which clearly show the shift of the peak from the remaining layer to negative values of mismatch. By comparing consecutive curves, the intensity due to the material just removed was determined and the average mismatch for that region was calculated. These data are summarized in Fig. 18, which conclusively shows the mismatch varying through the layer in the manner predicted by Fig. 14.

## G. Effect of Growth Solution Dope

In order to obtain practical device structures, doped quaternary layers are required. When dopants are added to a melt that is of the proper

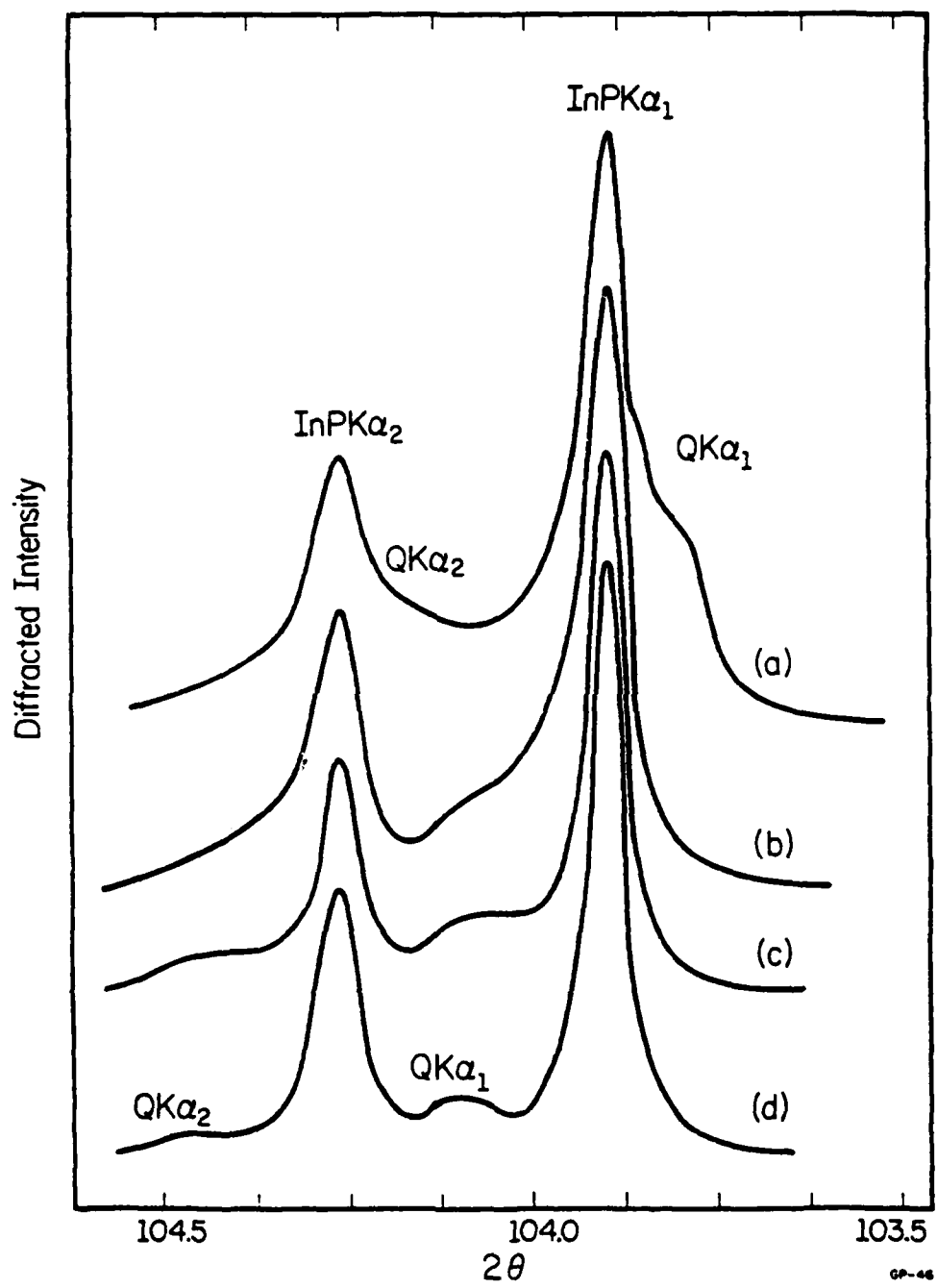


Figure 17. (600) diffraction curves of an InGaAsP layer grown by the equilibrium cooling technique after the layer was etched for progressively longer times from (a) to (d). Curve (a) is for the as grown 4.0  $\mu\text{m}$  thick layer ( $\Delta a/a = 0.06\%$ ), (b) after 1.5  $\mu\text{m}$  has been etched ( $\Delta a/a = -0.04\%$ ), (c) after 2.1  $\mu\text{m}$  was etched ( $\Delta a/a = -0.09\%$ ), and (d) after 2.7  $\mu\text{m}$  was etched ( $\Delta a/a = -0.13\%$ ).

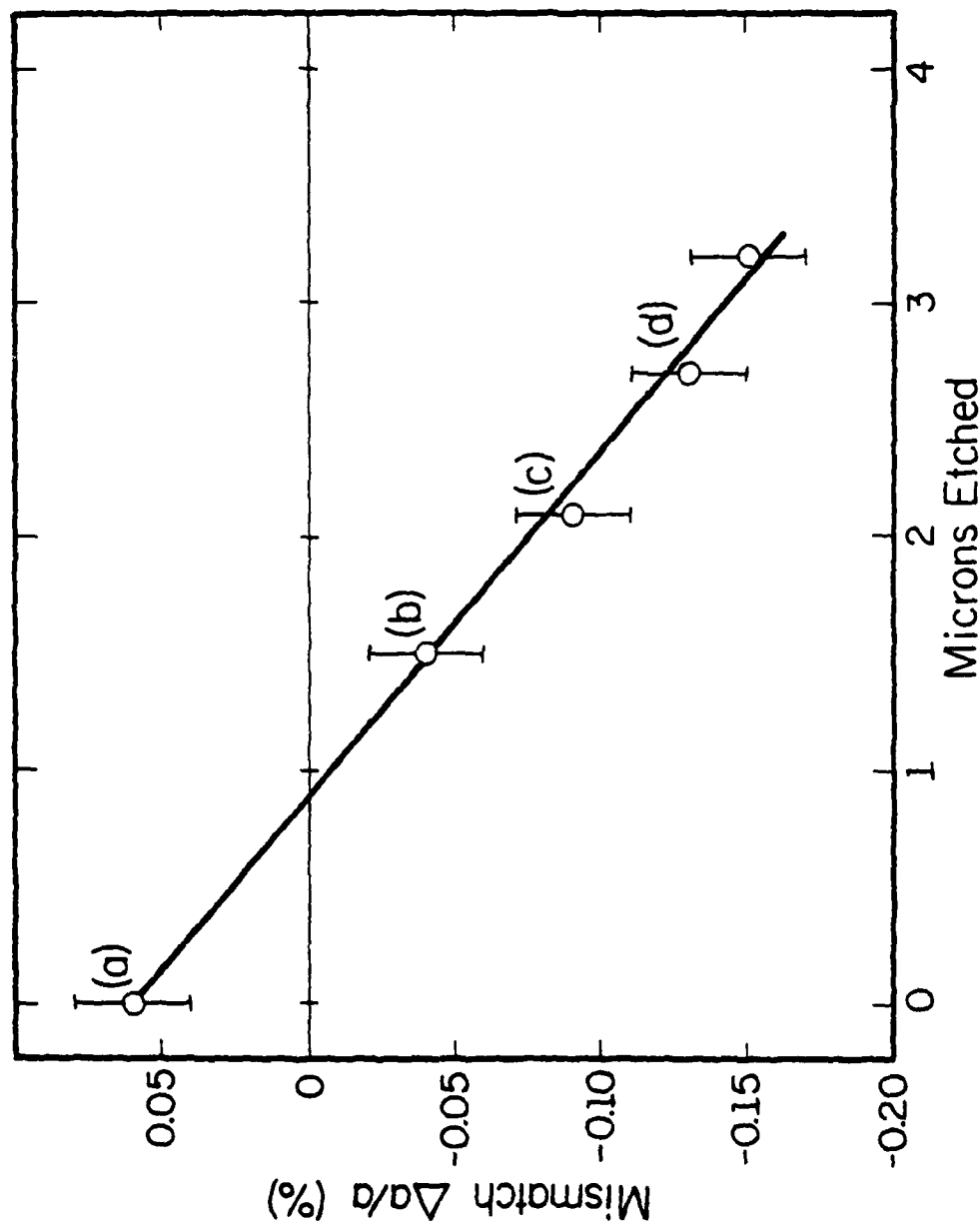


Figure 18. Variation of the lattice mismatch as a function of the amount of the layer that has been removed. The labeled points correspond to the curves in Fig. 17.

composition to produce a lattice matched unintentionally doped layer ( $N_D - N_A \leq 3 \times 10^6 \text{ cm}^{-3}$  as determined by Hall effect measurements), both the lattice match and  $\lambda_g$  can be disturbed.<sup>13,14</sup>

The effect of the n-type dopant Te is shown in Fig. 19. As the atomic fraction,  $X_{\text{Te}}^\lambda$ , is increased, from the smallest amount that can be accurately weighed, the lattice mismatch decreased from a significant positive mismatch. The band-gap wavelength,  $\lambda_g$ , determined by the transmission method neglects any band filling and/or band tailing effects. In this case,  $\lambda_g$  decreases continuously as  $X_{\text{Te}}^\lambda$  increases. The net donor density covered in Fig. 19 is from  $4 \times 10^{18}$  to  $5 \times 10^{19} \text{ cm}^{-3}$ .

The effect of the p-type dopant Zn on two different melt compositions is shown in Fig. 20. One set of curves is for the melt composition that would result in a lattice matched undoped layer. For this dopant, a lattice matched layer with the desired bandgap wavelength is produced when the smallest possible amount of Zn was added. As the amount of Zn in the melt is increased, the mismatch increased to +0.08% then decreased rapidly to a value of -0.15%. The band-gap wavelength also exhibited a similar behavior, first increasing then decreasing rapidly. The range of net acceptor concentration in Fig. 20 was from  $9 \times 10^{18}$  to  $4 \times 10^{19} \text{ cm}^{-3}$ .

The melt composition for the second set of curves was chosen to produce an undoped layer that would have had a lattice mismatch of +0.18% through a decrease in  $X_{\text{Ga}}^\lambda$ . The lattice mismatch is shifted to larger values (but not in a simple additive manner) decreasing from a value of +0.28% to +0.09%, while  $\lambda_g$  decreases from 1.20  $\mu\text{m}$  to 1.125  $\mu\text{m}$  over the indicated range of  $X_{\text{Zn}}^\lambda$ . This suggests that it is possible to compensate for the dopant effect by a judicious choice of melt composition that would produce the correct amount of mismatch in an undoped layer.

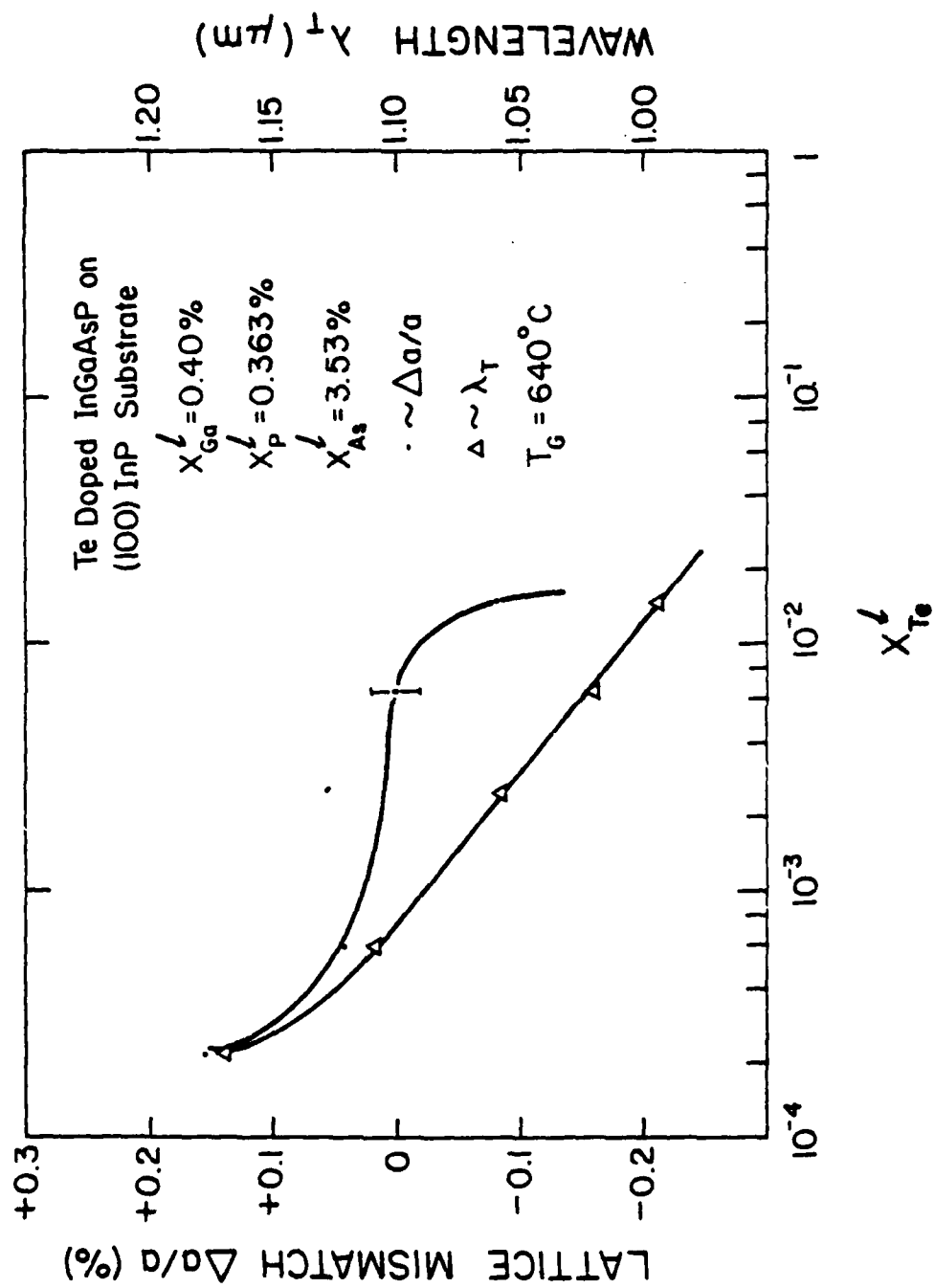


Figure 19. The variation of the lattice mismatch and transmission measurement wavelength,  $\lambda_T$ , as a function of  $X_{Te}^L$ .

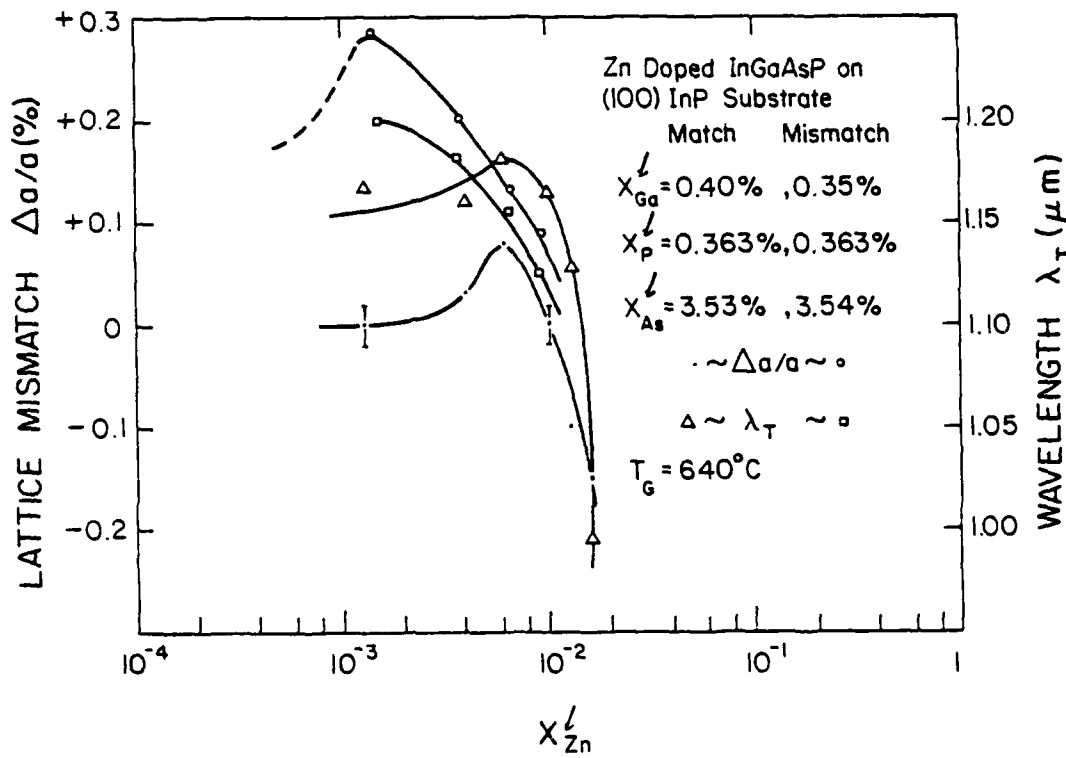


Figure 20. The variation of the lattice mismatch and  $\lambda_T$  as a function of  $X_{Zn}^\lambda$  for two different melt compositions.

## H. Interfacial Grading

### 1. Auger depth profiling

This report has demonstrated that high quality InGaAsP epitaxial layers can be grown by LPE under the proper conditions, however, the characterization methods used yield little information about the interfacial region forming the heterojunction between materials of differing composition. Therefore, Auger depth profiling was used to study the abruptness of the chemical interface of LPE grown heterojunctions.<sup>15,16</sup> The Auger depth profiling technique has been used by other workers to determine the interface width of LPE AlGaAs/GaAs heterojunctions which was found to be less than 130 Å.<sup>17</sup>

The Auger depth profiles were obtained using a Physical Electronics Incorporated Model 545 scanning Auger microprobe. Samples were mounted on a standard carousel with a 30° grazing incidence to the primary 5-keV electron beam. The target current with secondary-electron suppression was adjusted to ~16  $\mu$ A for all analyses. At the beginning of each analysis, the sample chamber residual vacuum was less than  $1 \times 10^{-9}$  Torr. Depth profiling was performed by sequentially monitoring the derivative peak-to-peak signals for the Auger transitions: In, 404; Ga, 1070; As, 1228; and P, 120 eV during simultaneous 3 or 1 keV  $\text{Ar}^+$ -ion bombardment for removal of successive atomic layers.

### 2. Effect of lattice mismatch

In the first study, the influence of lattice mismatch on the abruptness of LPE InGaAsP/InP/InGaAsP heterojunctions was studied. The samples were grown at 640°C by the step cooling technique on (100)-InP substrates, and the lattice mismatch was controlled by varying the amount of As in the

quaternary growth solution. The melt compositions for the three samples were  $X_{\text{Ga}}^l = 0.40\%$ ,  $X_{\text{P}}^l = 0.36\%$ , and  $X_{\text{As}}^l = 3.53\%$  (sample 313,  $\Delta a/a \leq \pm 0.03\%$ ),

3.40% (sample 314,  $\Delta a/a = -0.11\%$ ), 3.78% (sample 292,  $\Delta a/a = +0.20\%$ ).

The initial InGaAsP layer was grown for a period of 5 minutes followed by the sequential growth of InP and InGaAsP layers for a period of 7 seconds each. The last two layers were each about 1500 Å thick. The lattice mismatch was determined from the (600) diffraction peak of the thick quaternary layer.

Figure 21 shows the Auger depth profile for the lattice matched sample (313). There is essentially no difference in the chemical interface width, defined as the distance between the point where the Ga and As signals change between 10 and 90%, between the InP/InGaAsP and InGaAsP/InP heterojunctions. It should be noted that the Auger intensities of the quaternary constituents do not match very well on either side of the InP layer, contrary to what would be anticipated. This is attributed to the complexities in making quantitative determinations with the Auger profiling technique. However, Fig. 21 can be used as a reference for making comparisons with similar structures as was done here.

Figure 22 shows the Auger profile for sample 314 which had a larger mismatch ( $\Delta a/a = -0.11\%$ ) between the InP and quaternary layers than sample 313. In this case, the InGaAsP/InP interface width is essentially the same as in Fig. 21, however, the InP/InGaAsP interface shows considerable broadening. The Auger profile for sample 292, which has the largest amount of mismatch ( $\Delta a/a = +0.20\%$ ), is shown in Fig. 23. The InP/InGaAsP interface has an even greater width and there also appears to be some broadening in the InGaAsP/InP interface.

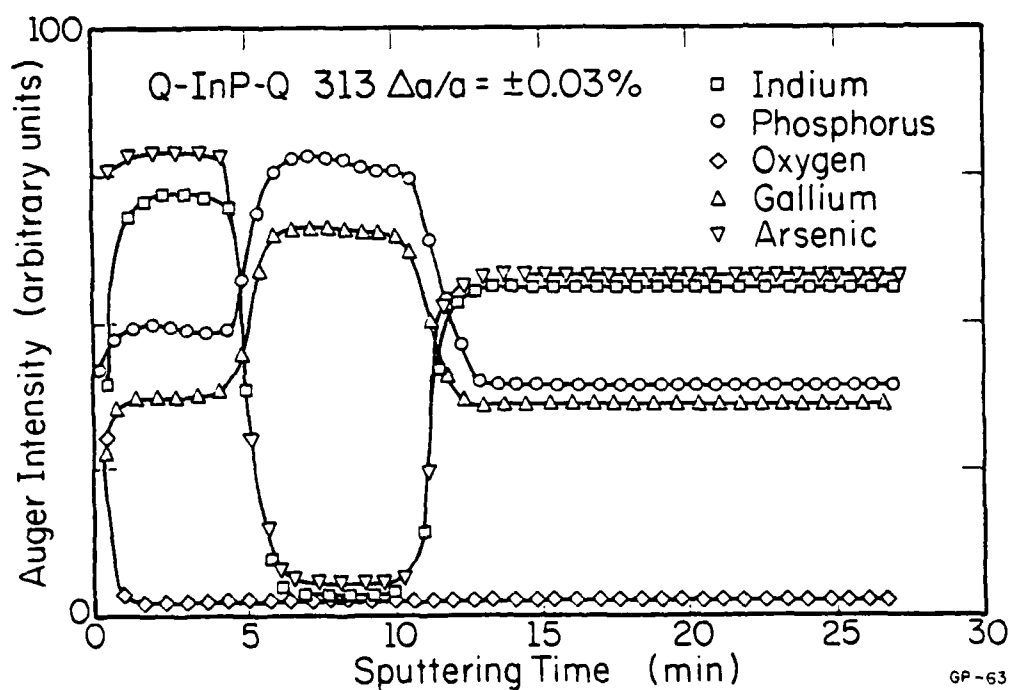


Figure 21. Auger depth profile of an InGaAsP/InP/InGaAsP heterostructure where the  $\lambda_g = 1.15 \mu\text{m}$  quaternary is closely lattice matched to the InP.

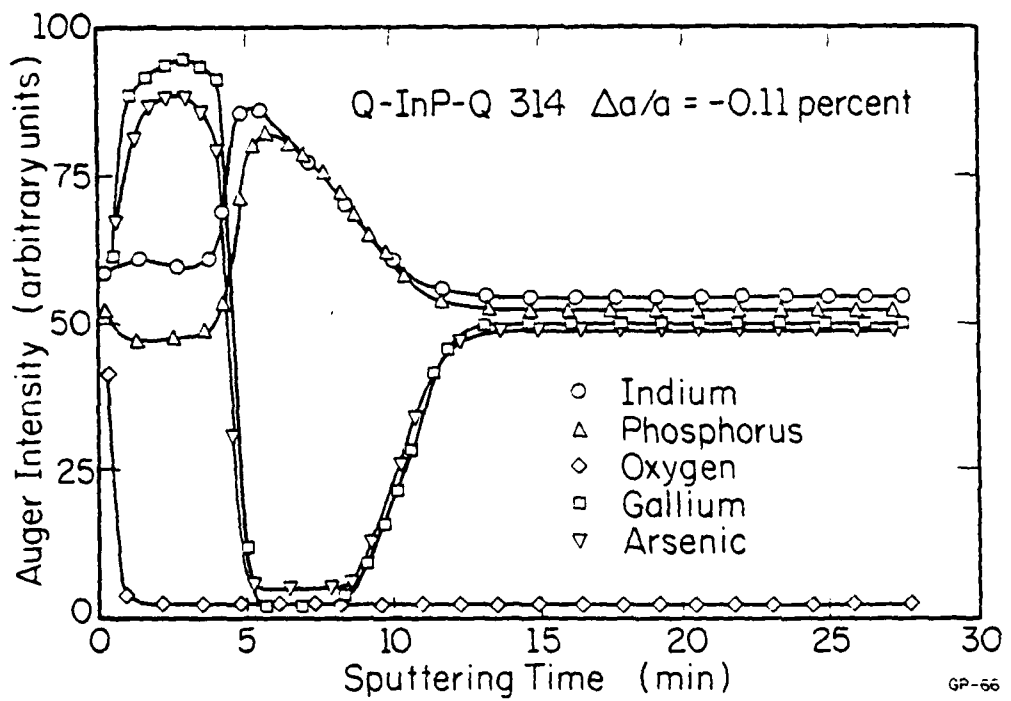


Figure 22. Auger profile of an InGaAsP/InP/InGaAsP heterostructure where the lattice mismatch between the quaternary and InP is - 0.11%.

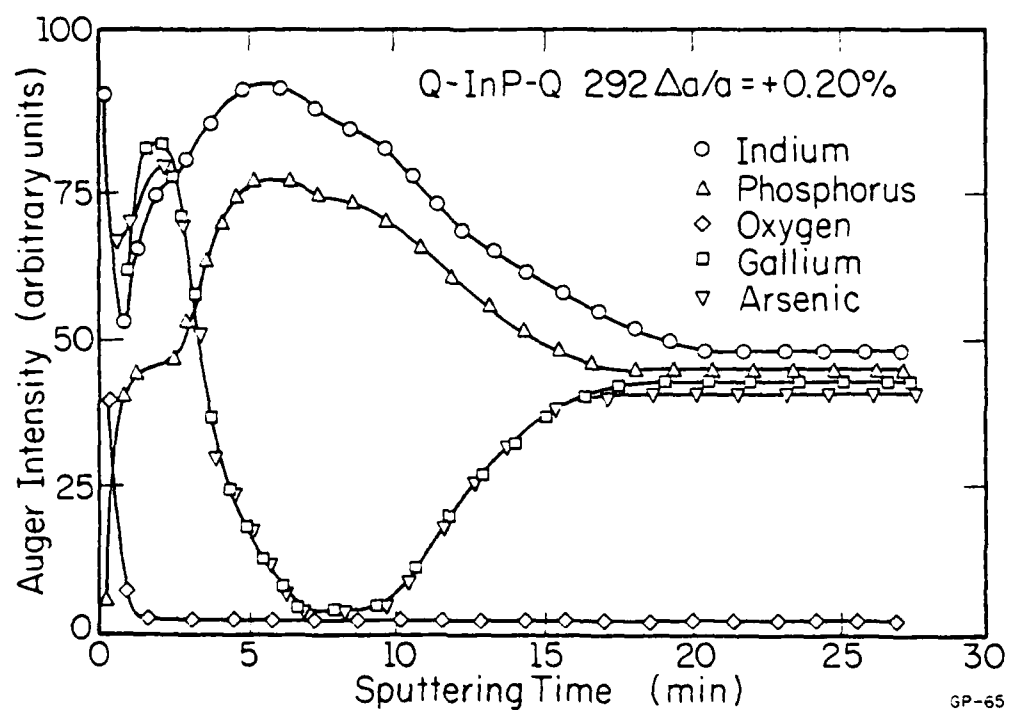


Figure 23. Auger profile of an InGaAsP/InP/InGaAsP heterostructure where the lattice mismatch is +0.20%.

These profiles clearly indicate that the grading of the InP/InGaAsP interface is more pronounced for larger values of mismatch. This observation can be explained by the growth kinetics of the interface.<sup>18</sup> The supersaturation of the growth solutions provides the driving force for nucleation at the interface, and the crystal growth that occurs is that which minimizes the free energy, including the surface energy. Any lattice mismatch will increase the surface energy and thus slow down the nucleation and growth for a given supersaturation of the growth solution. Thus, the lattice mismatch will result in greater dissolution of the quaternary and a wider graded composition interface region.

These results indicate that a close lattice match is required to fabricate InGaAsP/InP heterostructures by LPE and that a small amount of mismatch will cause significant grading, especially in InP/InGaAsP heterojunctions. Any grading at the interface can introduce additional strain, misfit dislocations, and other defects which can have disastrous effects on device performance.

### 3. Effect of dissolution

Another Auger profile study was performed on lattice matched InGaAsP/InGaAs/InGaAsP heterostructures to investigate the effects of dissolution.<sup>19</sup> The structure consisted of a 2  $\mu\text{m}$  quaternary ( $\text{In}_{1-x}\text{Ga}_x\text{As}_P$ ,  $x = 1.15$   $\mu\text{m}$ ) on a (100)-InP substrate followed by 500  $\text{\AA}$  of ternary and 1000  $\text{\AA}$  of quaternary. These lattice matched layers were grown by step cooling at a growth temperature of 640°C for the quaternary and 627.5°C for the ternary. The Auger profile of this structure, which is shown in Fig. 24, indicates that the InGaAs/InGaAsP interface has a width no greater than 90  $\text{\AA}$  (the resolution limit of the Auger microprobe) but that the InGaAsP/InGaAs

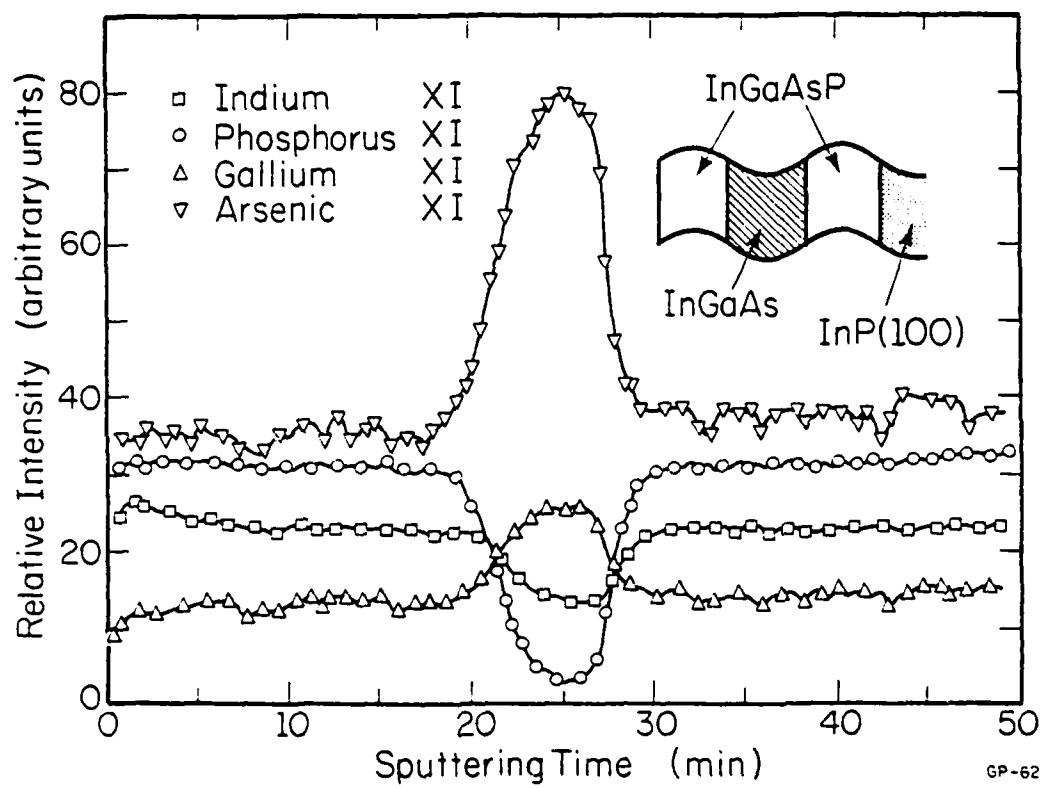


Figure 24. Auger profile of an InGaAsP/InGaAs/InGaAsP heterostructure showing the effects of dissolution at the InGaAsP/InGaAs interface.

interface is broadened. It might be expected that there would be some dissolution of the InGaAsP layer by the InGaAs growth solution because it is not saturated with phosphorus, however, it is the InGaAs layer which is slightly dissolved by the InGaAsP melt, as indicated by the broadening of the InGaAsP/InGaAs interface shown in Fig. 23. In general, there is significant dissolution of a layer if it has a higher arsenic concentration relative to the layer that is to be grown upon it.

The reason arsenic is so influential in the dissolution process is due to its higher diffusivity in In melts relative to the other components.<sup>16</sup> Therefore, arsenic controls the dissolution at the growth interface, which explains the interfacial compositional grading that occurs at the interface of a short-wavelength quaternary or InP layer and a longer wavelength quaternary or ternary layer. This conclusion indicates the difficulty of growing such structures by LPE.

## IV. MINORITY CARRIER DIFFUSION LENGTHS

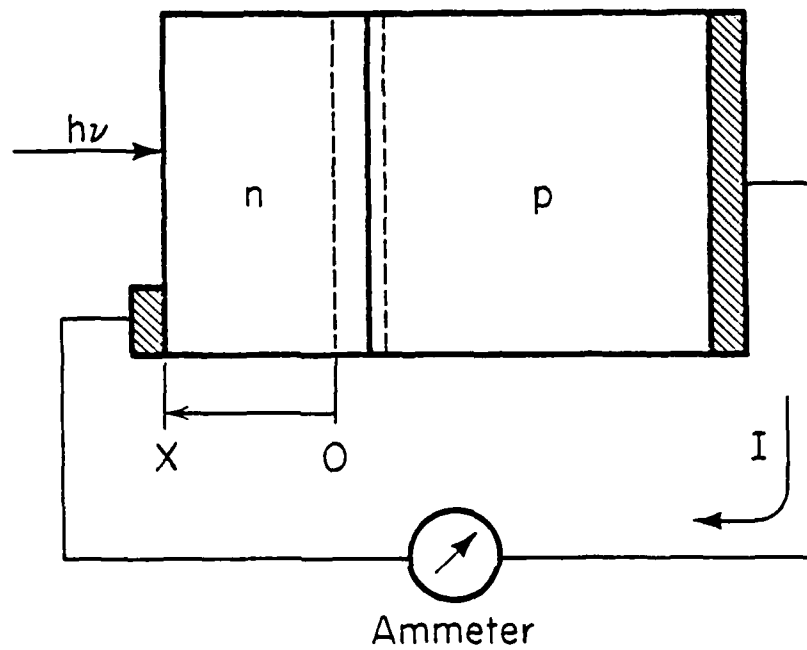
A. Introduction

The minority carrier diffusion length,  $L$ , is an important material parameter of quaternary and ternary epitaxial layers because it governs the distribution of carriers for devices relying on minority carrier injection and diffusion, and thus plays an important role in device performance and design. It is also an indication of the quality of the semiconductor. This section of the report covers some of the theory required to interpret the experimental data and a description of the diffusion length measurement technique, and presents results on the effect of lattice mismatch on the hole diffusion length ( $L_p$ ) of n-type LPE InGaAsP ( $\lambda_g = 1.15 \mu\text{m}$ ) and the variation of the electron diffusion length ( $L_n$ ) with hole concentration for Zn-doped lattice matched InGaAsP ( $\lambda_g = 1.15 \mu\text{m}$ ) and InGaAs epitaxial layers grown by LPE. Preliminary results on hole diffusion lengths of n-type InP grown by vapor phase epitaxy (VPE) are also presented.

B. Theory of the Measurement

The diffusion length is obtained by measuring the variation of the short-circuit photocurrent produced by a light spot as it is scanned across a bevelled p-n junction. Therefore, this section covers a theoretical treatment of how the photocurrent is affected by the parameters of most influence: surface recombination velocity ( $S$ ), distance of the light spot from the junction ( $x$ ), minority carrier diffusivity ( $D_p$ ), and the absorption coefficient ( $\alpha$ ) in order to gain an understanding of the photocurrent data generated by the measurement.

The equation for the short circuit current due to the illumination of a p-n junction diode can be obtained by using the model in Fig. 25. Light



LP-1678

Figure 25. The circuit model used to calculate the solution for the short circuit current due to minority carrier diffusion.

of wavelength,  $\lambda$ , is incident from the n side. The distance from the surface to the edge of the depletion region is denoted by  $x$ . The differential equation for the excess minority carrier density,  $p$ , in the n-type region is:

$$\alpha N_0 (1 - R) e^{-\alpha x} + D_p \frac{d^2 p}{dx^2} - \frac{p}{\tau_p} = 0$$

The first term describes the generation of electron-hole pairs by the light source,  $N_0$  denotes the incident photon flux,  $(1 - R)$  is the transmittance, and  $\alpha$  is the absorption coefficient for the particular wavelength of light illuminating the sample. The second term represents the change in hole density due to diffusion where  $D_p$  is the hole diffusivity. The last term is the loss of minority carriers due to recombination, and  $\tau_p$  is the minority carrier lifetime. The contribution to the current due to electrons generated within the p-type region is properly neglected since the absorption coefficients of the quaternary and ternary for the wavelength of light used in the experiment are large.

The solution of this equation with the boundary conditions  $p(0) = 0$  at the junction and  $dp/dx = S_p(x)/D_p$  at the surface gives the current from the concentration gradient of the hole density at the depletion region edge.<sup>20</sup> The normalized short-circuit current is plotted semilogarithmically in Figs. 26-29 where the effect of one parameter is displayed while the others are maintained constant. The "standard" values for these variables are  $S = 10^5$  cm/s,  $D_p = 10$  cm<sup>2</sup>/s,  $\alpha = 10^5$  cm<sup>-1</sup>, and  $L_p = 2$   $\mu$ m. The primary characteristic of the solution for the current is that under certain conditions, namely,  $\alpha$  large and  $x > L_p$ , the solution reduces to a simple exponential decay,  $I \propto e^{-x/L_p}$  ( $L_p = \sqrt{D_p \tau_p}$ ).

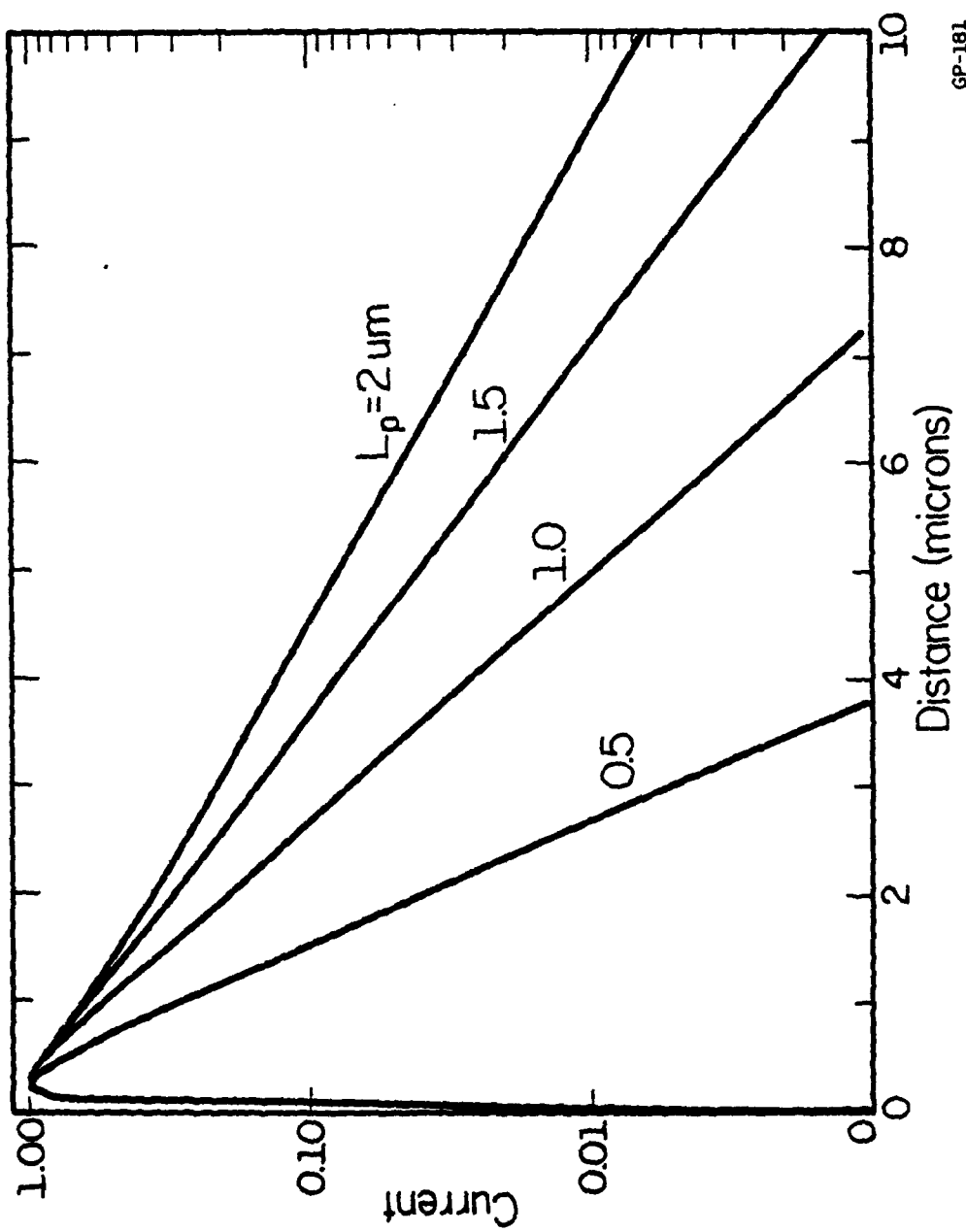


Figure 26. Effect of the diffusion length on the short circuit current.

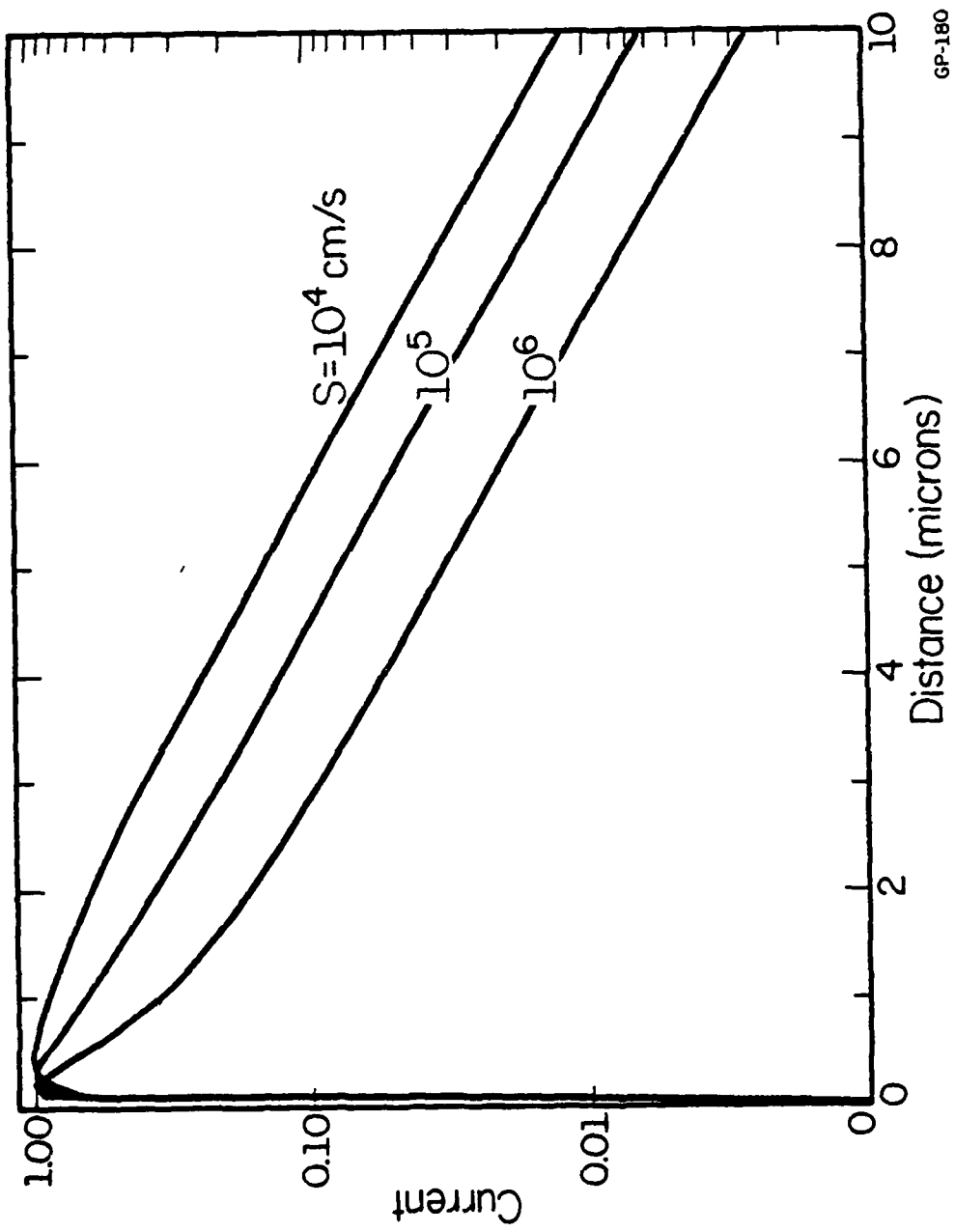


Figure 27. Effect of surface recombination on the short circuit current.

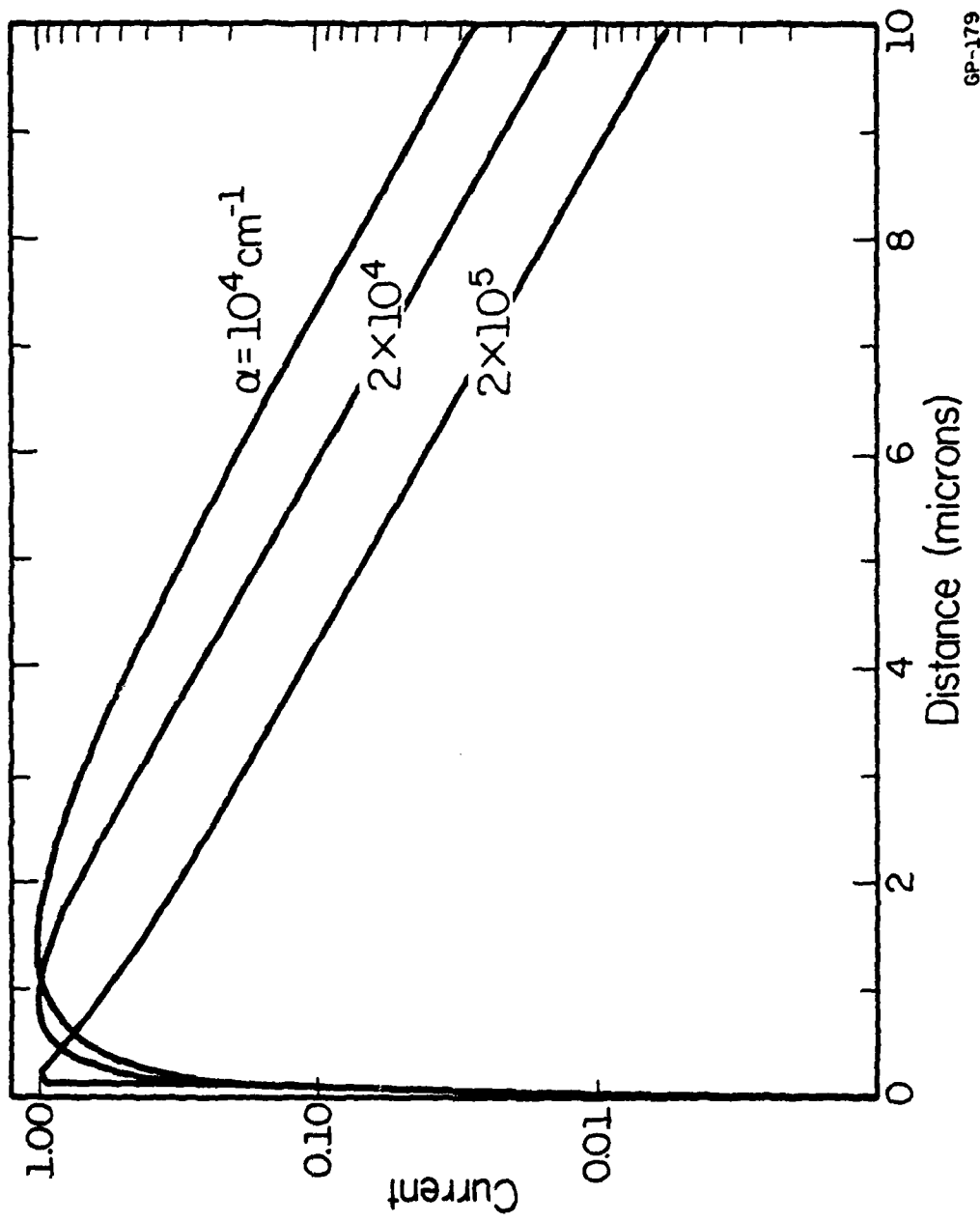


Figure 28. Effect of the absorption coefficient on the short circuit current.  
GP-179

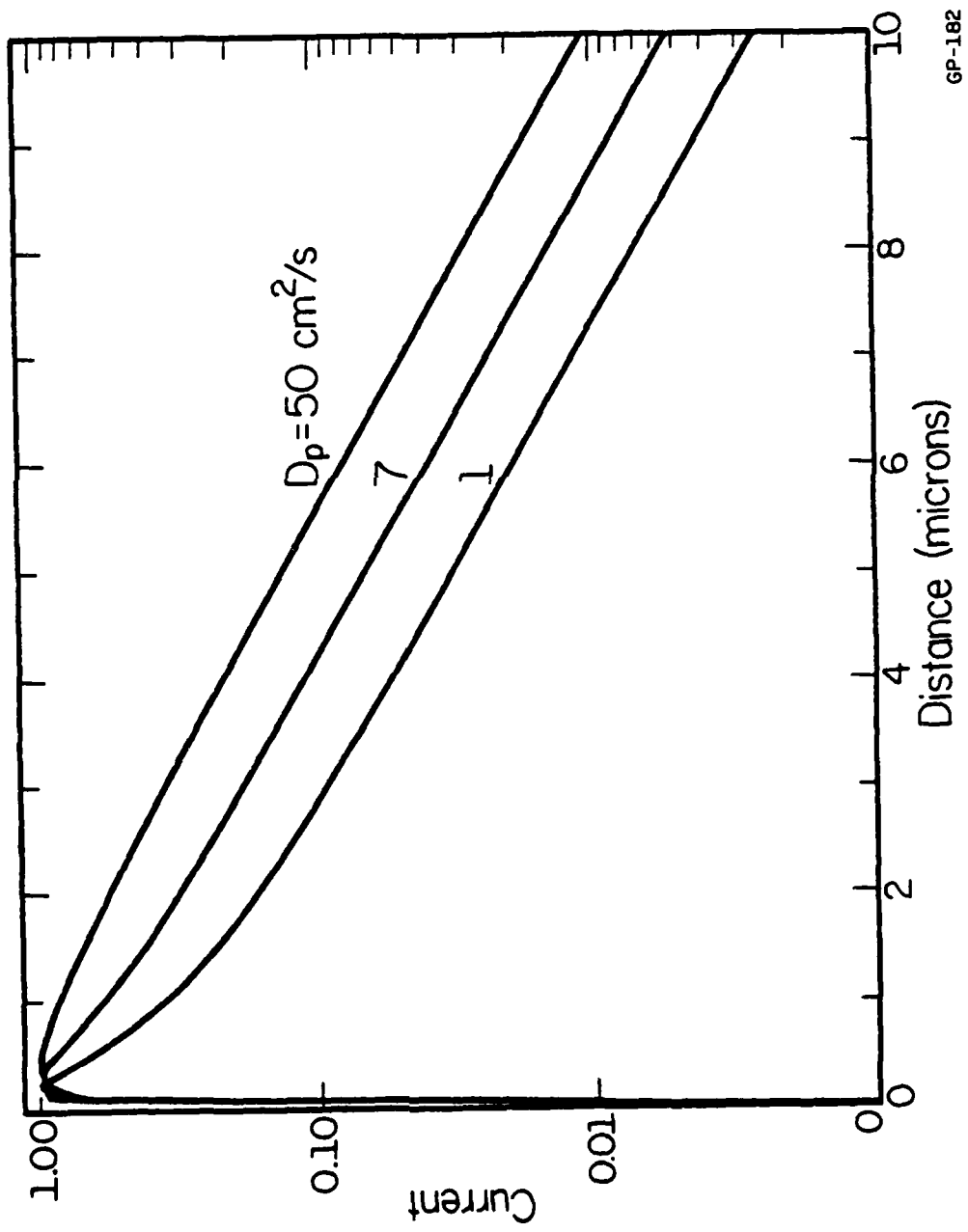


Figure 29. Effect of the minority carrier diffusivity on the short circuit current.

In Figure 26, the uppermost curve is for the "standard" conditions. Note that in this curve (and all that appear) the current is zero at the junction; this is due to the implicit assumption that the depletion region contributes no current, which is clearly faulty. However, since the measurement relies on data far from the junction, the assumption is valid for obtaining the diffusion length. The most important feature of this curve is the linear decay of the logarithm of the current as the distance from the junction increases. The slope of the linear portion of the curve yields a diffusion length of  $2 \mu\text{m}$ , the "standard" value. As the diffusion length becomes shorter, the slope becomes steeper. For short diffusion lengths, the change in slope is very pronounced, making the scanned light spot diffusion length measurement ideal for semiconductors with short diffusion lengths, which are typical of many direct bandgap compound semiconductors.

The next three plots show how the curves are influenced by the variation of one of the parameters:  $S$ ,  $D_p$ , or  $\alpha$ . The motivation for this is to establish how far from the junction the light spot must be before the linear portion of the curve begins, which indicates the minimum thickness the layer must have to make a reliable interpretation of the photocurrent data. Figure 27 shows the variation of the surface recombination velocity. The principal effect is how  $S$  influences the current near the junction. As  $S$  increases, the drop in current from its maximum value increases due to the loss of carriers at the surface. Also after about  $2.5 \mu\text{m}$ , the linear characteristic is displayed for all these values of  $S$  for a  $2 \mu\text{m}$  diffusion length.

The effect of the absorption coefficient on the current depicted in Fig. 28 is similar to that of  $S$  since it determines where the minority

carriers are generated; as  $\alpha$  increases, the carriers are generated in closer proximity to the surface. For a reasonable value of  $\alpha (> 2 \times 10^4 \text{ cm}^{-1})$ , the plots indicate that after one diffusion length the curves become linear.

The curves in Fig. 29 are plots with the minority carrier diffusivity as the free parameter. These curves also indicate that for reasonable values of  $D_p (= 10 \text{ cm}^2/\text{s})$  a linear variation is obtained after one diffusion length. In summary, these figures demonstrate that the thickness of the n-type layer should be at least two times thicker than the measured diffusion length in order to obtain an exponential decay of the photocurrent.

### C. Experimental Procedures

#### 1. Crystal growth

The InGaAsP quaternary and InGaAs ternary layers were grown by liquid phase epitaxy. The n- and p-type layers were grown on Zn and Sn-doped (100)-InP substrates, respectively, to form a grown p-n junction. The proper amounts of GaAs, InAs, InP (for the quaternary layers), and Zn (in the form of a dilute Zn-In alloy) for the doped layers were added to 1.2 g of In to form melts saturated at 650°C for the quaternary and 630°C for the ternary. Prior to growth, the substrate was etched in a pure In melt to remove thermal damage. The layers were grown at a constant temperature of 640°C for the quaternary and 627.5°C for the ternary for approximately 25 minutes.<sup>19</sup>

In the lattice mismatch experiment, the amount of lattice mismatch of the layers was adjusted by varying the atomic fraction of Ga in the melt, since this produces a large change in the lattice mismatch with little change in the bandgap energy.<sup>8</sup> For the p-type doped layers ( $p \leq 1 \times 10^{17} \text{ cm}^{-3}$ ), the melts were baked at 665°C and 650°C for the

quaternary and ternary layers, respectively, for about 35 hours in order to reduce the background electron concentration of the layers before the substrate and dopant were loaded into the boat.

From previous optical transmission measurements,<sup>19</sup> the wavelength  $\lambda_g$ , corresponding to the bandgap energy for the lattice-matched updoped quaternary and ternary layers, was determined to be 1.15 and 1.68  $\mu\text{m}$ , respectively. The lattice mismatch was determined by x-ray diffraction measurements on the as grown samples at room temperature using the horizontal single crystal diffractometer. A symmetric diffraction geometry was used, therefore, the measured mismatch was the component perpendicular to the surface.

The VPE n-type InP layers were grown on Zn doped (100)InP substrates misoriented by 3° to the <110> direction by the hydride technique.<sup>20</sup> The effect of the source temperature ( $T_s$ ) at the In boat on the hole diffusion length was investigated.

## 2. Wafer processing

The first processing step in the fabrication of the measurement structure is the deposition of a 3000 Å thick film of pyrolytic  $\text{SiO}_2$  on the epitaxial layer to protect the surface during the subsequent steps and to serve as a mask for the contact pattern. The substrate is then lapped with a coarse grit abrasive slurry to remove the thermal damage produced during the growth and make the backside of the wafer parallel to the surface of the epitaxial layer. An ohmic contact is formed on the entire back surface by electroplating and then alloying at ~400°C either AuSn or AuZn alloys for n- or p-type substrates, respectively. A pattern of 200  $\mu\text{m}$  diameter contact dots is produced photolithographically on the oxide, and ohmic contacts are formed

in these dots by the same method used for the substrate contacts of the same conductivity type material. For the special case of the lightly doped p-type layers ( $p \leq 10^{16} \text{ cm}^{-3}$ ), a sandwich of AuZn/Zn/AuZn, which was electroplated and alloyed in the same manner, was required to insure the formation of ohmic contacts. After the contacts have been alloyed, a final plating of Au on both contact surfaces is performed to reduce the contact resistance and minimize the problems in making reliable electrical contact with the sample when it is probed.

A critical processing step for a successful measurement is angle lapping the layer to produce a nearly damage free surface. The contacted sample is mounted on a 1-inch diameter polishing plug which has been machined to a  $\sim 1^\circ$  angle. The leading and trailing edges of the wafer are protected by cleaved GaAs rails to prevent damage to these edges and resultant scratches on the lapped surface. For further protection, the mounting wax is built up around all the edges of the rails and sample. The sample is first lapped down roughly with a slurry composed of 5  $\mu\text{m}$  levigated alumina and deionized (DI) water on a ground glass plate to expose the layer. The final polishing steps are performed on a specially fabricated epoxy plate which has been filled with 0.3  $\mu\text{m}$  alumina.<sup>22</sup> The surface of the plate is finished by grinding it with 220 grit silicon carbide sandpaper mounted on a large glass disc.

The sample is first lapped on this plate with a 0.3  $\mu\text{m}$  alumina and DI water slurry until a fairly good surface with a few pits and scratches is produced. For the final step, a slurry composed of a solution of sodium hypochlorite (clorox), DI water and 0.3  $\mu\text{m}$  alumina is used while lapping until virtually all the surface defects are removed leaving a specular surface. Figure 30 is an optical micrograph of a typical lapped surface, in this case,

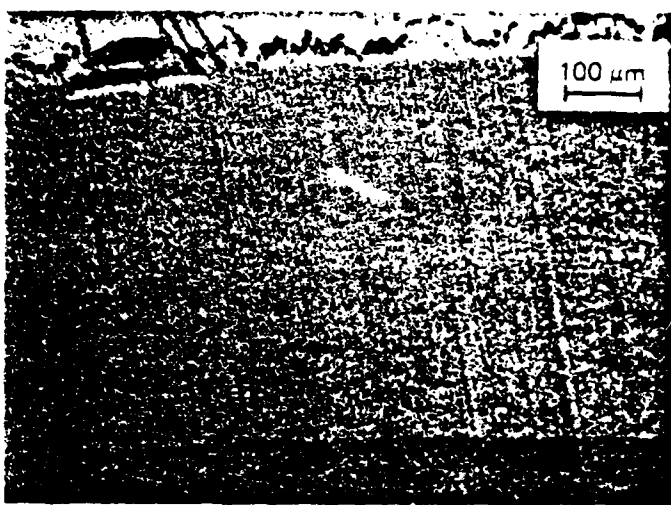


Figure 30. An optical micrograph of the angle-lapped surface of an InGaAs epitaxial layer.

an 8  $\mu\text{m}$  thick p-type InGaAs layer. The unlapped surface of the layer is at the top of the photograph while the lighter region below it is the ternary layer bounded at the bottom of the darker region which is the InP substrate. The small curvature of the InGaAs/InP interface is due to the slightly concave substrate surface produced when polishing the InP crystal prior to growth. Although a few pits and deep scratches remain, most of the area is usable for the measurement.

A pictorial rendition of a finished sample is shown in Fig. 31. In the diffusion length measurement, a light spot is scanned from the top surface down the bevel to the junction. The minority carriers generated by the absorption of the incident photons diffuse to the junction and are collected when they reach the edge of the depletion region producing the measured photocurrent, which is a function of the spot position on the surface. This position coordinate is transformed to the vertical distance the spot is from the junction with the knowledge of the angle the lapped surface forms with the unlapped top surface. The bevel angle is determined with a Dektak surface profilometer. A representative Dektak trace is shown in Fig. 32 which was taken for the sample shown in Fig. 30. The angle is found by taking the arctangent of the slope of the bevel. For this sample, the angle  $\theta$  was found to be  $0.82^\circ$ . After completion of the diffusion length measurements on a particular wafer, mesa etched diodes are fabricated from the unlapped portion of the sample shown in Fig. 31 and capacitance-voltage (C-V) measurements are performed to determine the majority carrier concentration of the layers.

### 3. Diffusion length measurement system

A block diagram of the diffusion length measurement system is shown in Fig. 33. The beveled sample is situated under the microscope objective

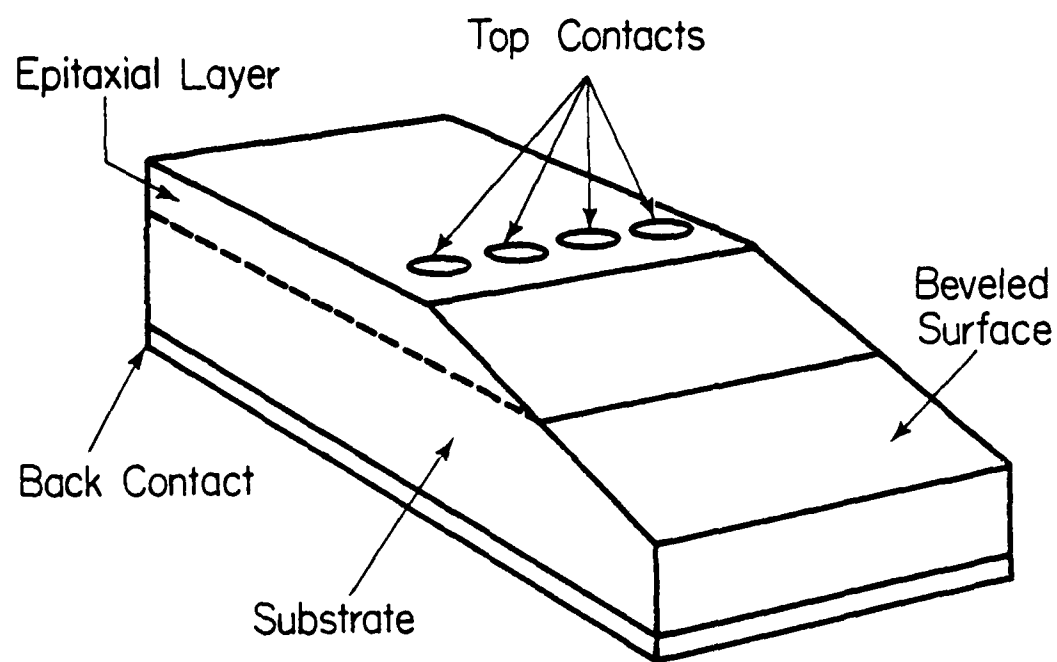


Figure 31. A pictorial representation of a sample used for the diffusion length measurement.

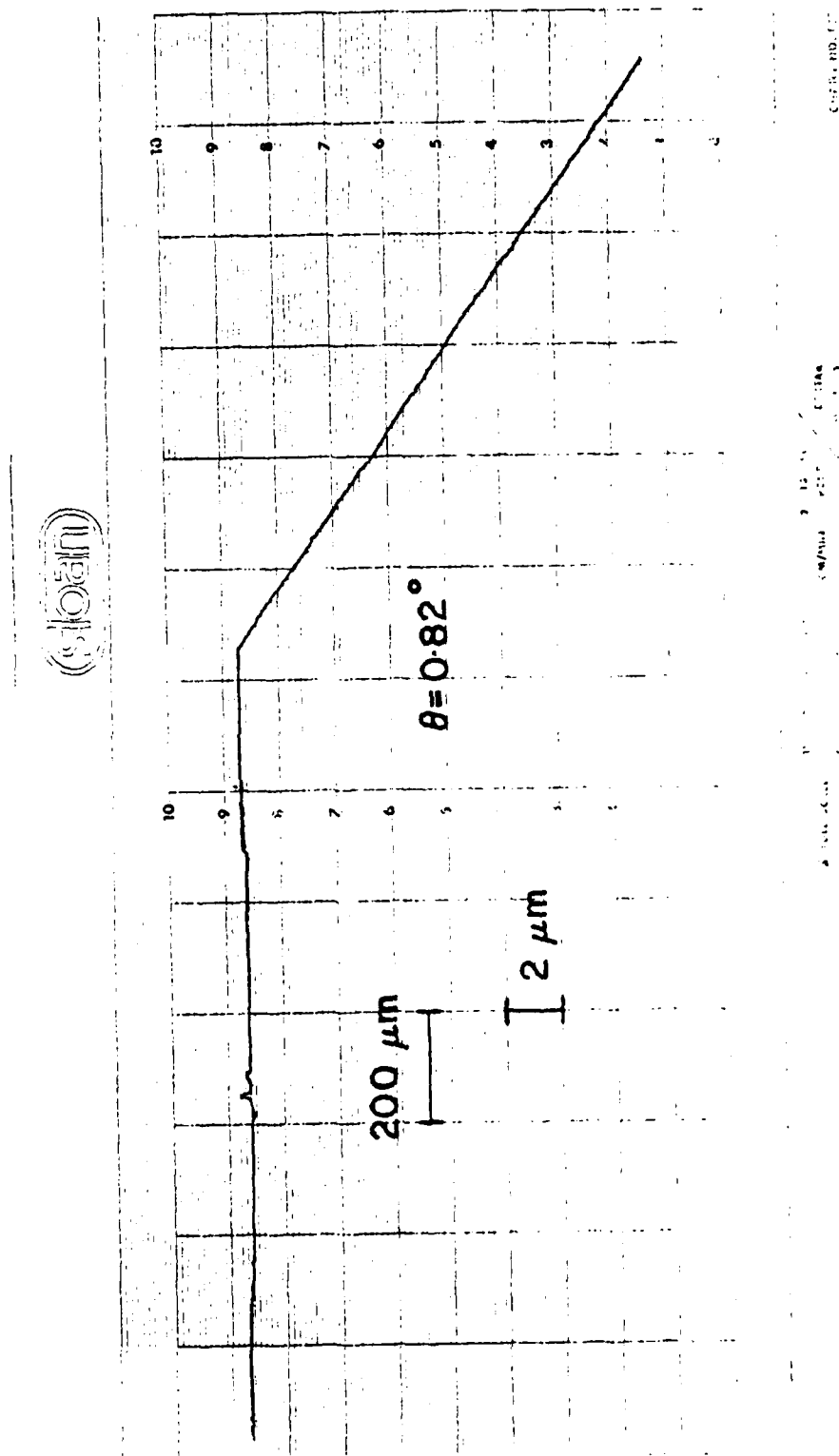


Figure 32. The Dektak surface profilometer scan of the sample in Fig. 30 used to determine the bevel angle,  $\theta$ .

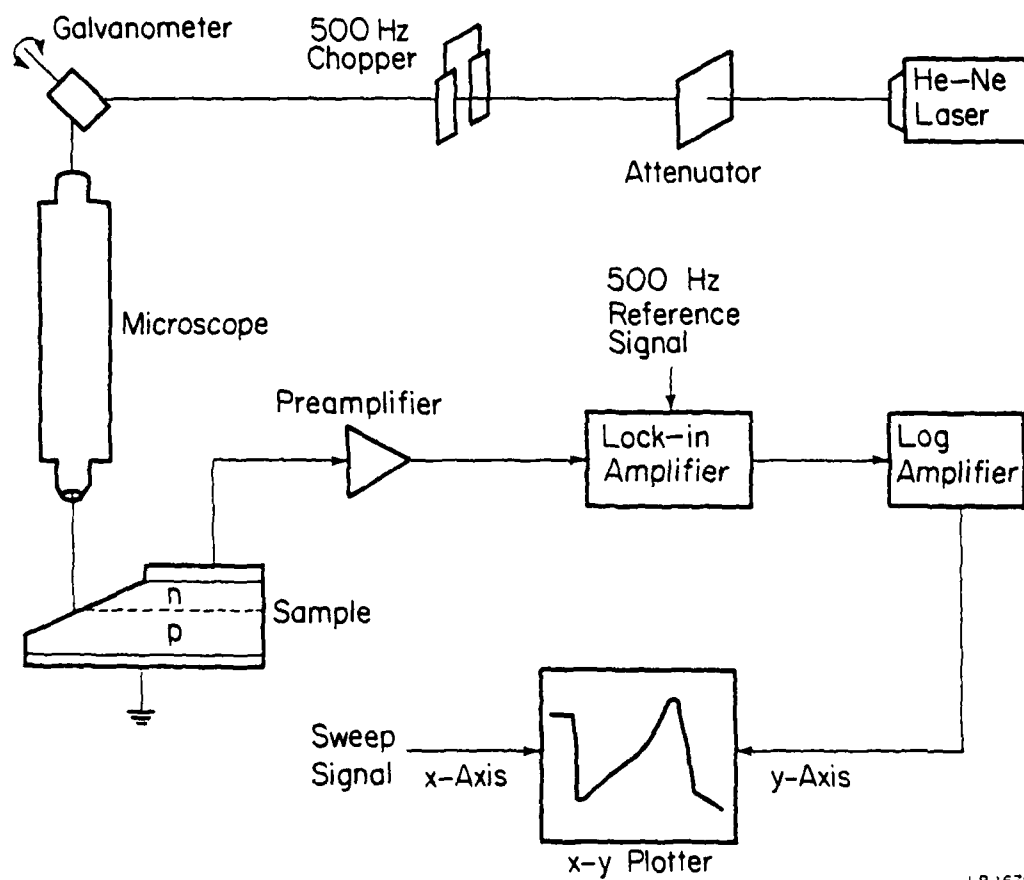


Figure 33. Schematic diagram of the diffusion length measurement system described in the text.

on a platform which serves to contact the substrate. The beam from a He-Ne laser ( $\lambda = 0.6328 \mu\text{m}$ ) is attenuated by neutral density filters and mechanically chopped at 500 Hz before it is directed through the microscope photoeyepiece by a mirror located near the exit pupil of the eyepiece. The diameter of the focussed light spot on the sample was visually estimated to be approximately 5  $\mu\text{m}$  for the objective used in this work, and the power incident on the sample was measured to be near 0.5  $\mu\text{W}$  by a radiometer. The light spot is scanned across the field of the microscope objective through the rotation of the galvanometer driven mirror by a slow linear ramp signal. The total distance scanned by the light spot is measured with a calibrated eyepiece reticle. The variation in the intensity of the light spot across the total scan length was verified to be less than  $\pm 2\%$  using a large area Si photodetector, with most of the measured variation occurring at the very beginning and end of the scan where it is least important.

A sample is aligned so that the scan direction is perpendicular to the visible junction line and is contacted with a 1 mil diameter wire probe. As the light spot is scanned across the sample, the short circuit photocurrent is amplified by a low noise current amplifier and detected by a lock-in amplifier. The logarithm of the output signal from the lock-in is recorded on the vertical axis of the x-y plotter while the horizontal axis of the plotter is swept in synchronism with the scanned light spot, generating a semilogarithmic plot of photocurrent as a function of the position of the light spot. A complete scan is shown schematically within the block representing the plotter for a scan starting from the top surface in a region between the contact dots and proceeding down the bevel, ending below the p-n junction where the laser beam is situated in the diagram. In this experiment,  $x$ , the distance from the surface to the edge of the p-n

junction depletion region is related to the horizontally scanned distance  $d$  by the relation  $x = dtan \theta$ . After  $\theta$  is measured, the vertical distance  $x$  can be determined for the semilogarithmic plot, and the diffusion length is computed from the linear portion of the response. The primary uncertainty in this measurement is the determination of the bevel angle because it is so small. With this consideration, the estimated error in the diffusion lengths is  $\pm 10\%$ . The variation in  $L$  about the average value for scans from different regions of a sample were within these limits.

The plot of a typical diffusion length scan is shown in Fig. 34. The current axis has been normalized by the peak value of the response which occurs at the p-n junction where the origin for the distance axis,  $x$ , is located. This particular sample was a  $7 \mu\text{m}$  thick InGaAsP epitaxial layer which was lattice matched and had an electron concentration of  $3 \times 10^{16} \text{ cm}^{-3}$ . The light spot was scanned from the bare epitaxial layer surface down the bevel to the p-n junction from left to right on the plot. The sharp step at the left of the plot is caused by the transition from the top unlapped surface to the lapped surface, and is due to a large difference in surface recombination velocity between the lapped and as grown surfaces. The slope of the linear portion of the plot yields an  $L_p$  of  $1.5 \mu\text{m}$ . The flat response between  $3.5$  and  $4 \mu\text{m}$  corresponds to that from the top of the bevel and is characteristic of this edge region produced by the lapping procedure. The  $4 \mu\text{m}$  thickness is less than the measured cross section layer thickness ( $7 \mu\text{m}$ ) because of the finite optical penetration depth of the light spot, the width of the depletion region, and a post growth annealing step which moved the junction into the n-type layer.<sup>23</sup>

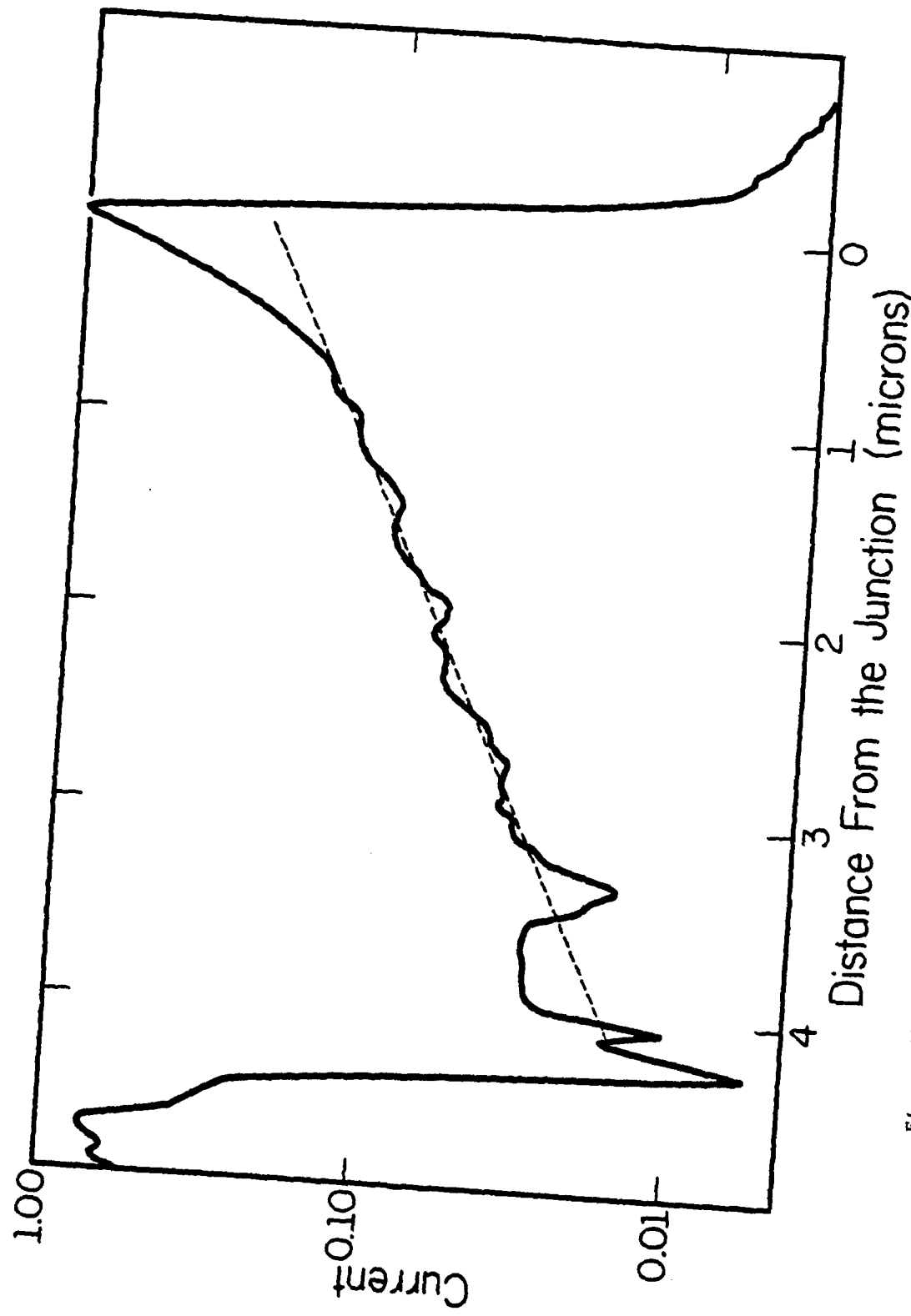


Figure 34. A plot of the logarithm of the normalized photocurrent versus light spot position produced by a typical diffusion length scan. The diffusion length determined from this scan (the dashed line) was  $L_p = 1.5 \mu\text{m}$ .  
LP-1847

#### D. Experimental Results

##### 1. Effect of lattice mismatch

The variation of the hole diffusion length with lattice mismatch of unintentionally doped InGaAsP epitaxial layers is shown in Fig. 35. The maximum diffusion length ( $L_p = 1.5 \mu\text{m}$ , Fig. 34) occurs when the epitaxial layer is lattice matched to the InP substrate. As the mismatch increases both positively and negatively,  $L_p$  decreases linearly. At the extreme mismatch values ( $\Delta a/a = +0.31\%$  and  $-0.25\%$ , with  $L_p = 0.9$  and  $0.84 \mu\text{m}$  respectively) the surface morphology is poor and cracking of the epitaxial layer was observed for the negative value of mismatch. The electron concentration for these layers, as determined from the C-V data, ranged from  $2 \times 10^{15}$  to  $5 \times 10^{16} \text{ cm}^{-3}$  and within this doping range there was no correlation between  $L_p$  and the variation of the electron concentration. The poor quality of the epitaxial layers at the extreme value of mismatch limits the range within which the scanned laser spot technique can be used, since a good p-n junction is required.

##### 2. Effect of hole concentration

Previous workers have reported electron diffusion lengths,  $L_n$ , between 1 and  $2 \mu\text{m}$  for heavily doped ( $p \approx 2 \times 10^{18} \text{ cm}^{-3}$ ) InGaAsP<sup>24,25</sup> and InGaAs<sup>25</sup> lattice matched layers.

The influence of the hole concentration of the electron diffusion length for Zn-doped lattice matched InGaAsP epitaxial layers is shown in Fig. 36.  $L_n$  decreases monotonically from  $3.5 \mu\text{m}$  at a hole concentration of  $3 \times 10^{15} \text{ cm}^{-3}$  to  $0.13 \mu\text{m}$  at  $p = 5 \times 10^{18} \text{ cm}^{-3}$ . The decrease in  $L_n$  with  $p$  is small until  $p = 10^{17} \text{ cm}^{-3}$  where it begins to decrease more rapidly with the hole concentration.

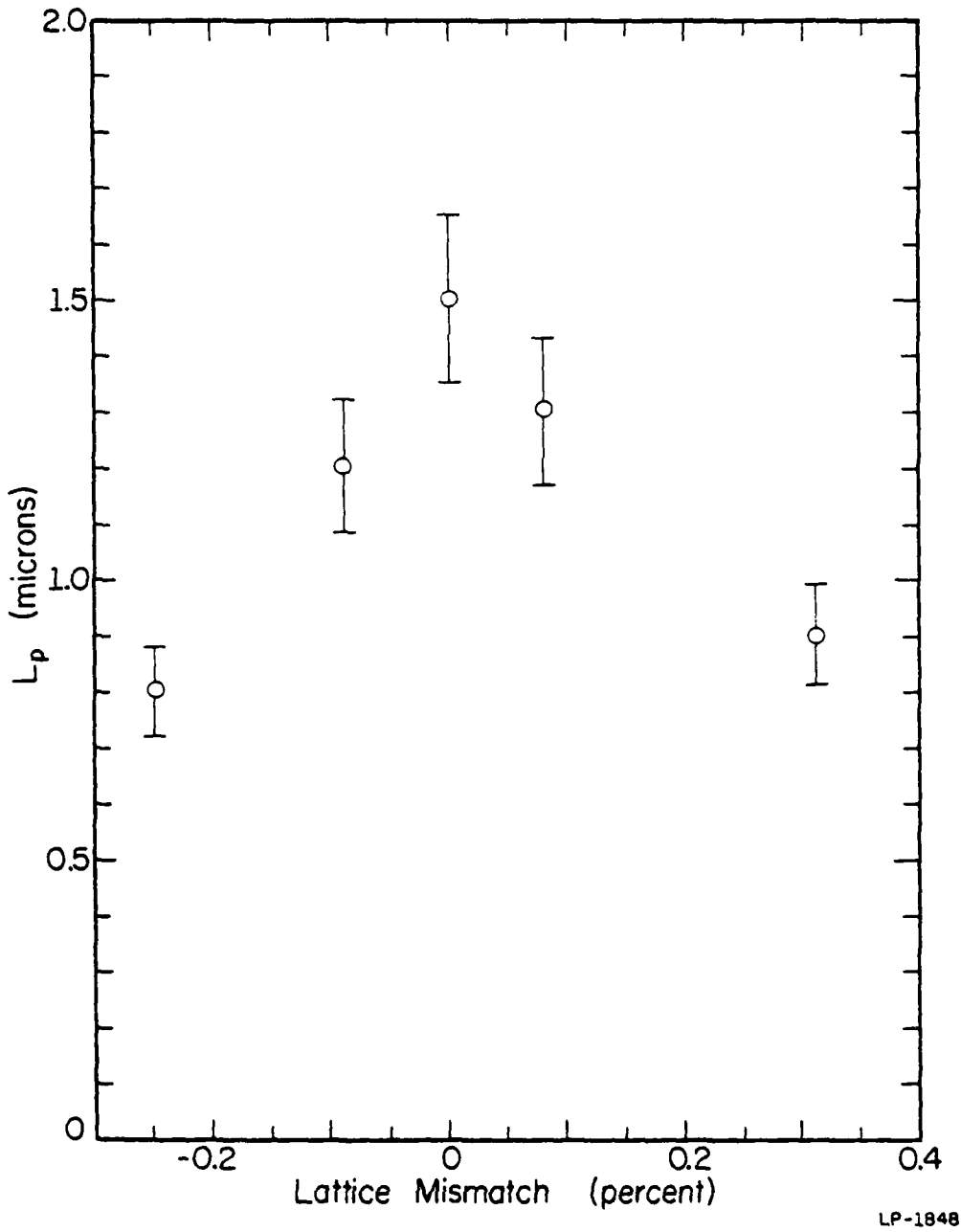


Figure 35. The variation of the hole diffusion length with lattice mismatch for InGaAsP ( $\lambda_g = 1.15 \mu\text{m}$ ).

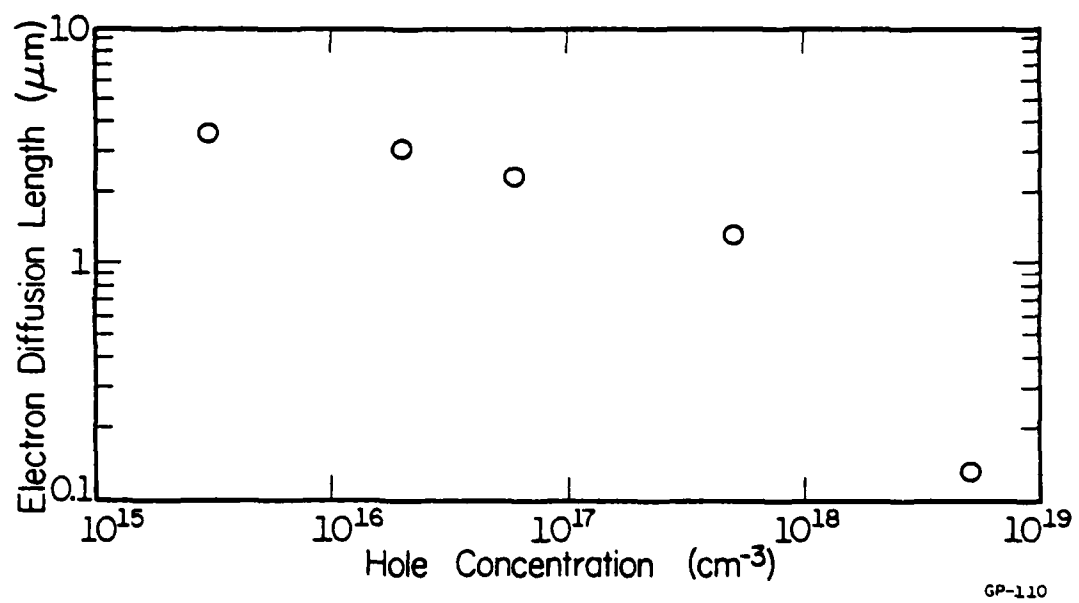


Figure 36. The variation of the electron diffusion length with hole concentration of InGaAsP ( $\lambda_g = 1.15 \mu\text{m}$ ).

GP-110

Similar behavior was observed for the p-type InGaAs layers as shown in Fig. 37. At the lowest hole concentration ( $p = 1.4 \times 10^{16} \text{ cm}^{-3}$ ) the electron diffusion length was  $2.5 \mu\text{m}$  and decreased to a value of  $0.83 \mu\text{m}$  at the highest concentration measured ( $p \sim 5 \times 10^{18} \text{ cm}^{-3}$ ). The point at which  $L_n$  in the ternary begins to drop rapidly with hole concentration occurs at  $p \sim 10^{18} \text{ cm}^{-3}$ , an order of magnitude higher than for the quaternary. A single data point for the hole diffusion length of an unintentionally doped unbaked n-type ternary layer is also shown on this plot for comparison ( $L_p = 2.4 \mu\text{m}$  for  $n = 6 \times 10^{15} \text{ cm}^{-3}$ ).

### 3. Effect of the source temperature on $L_p$ of VPE InP

The influence of the In boat source temperature on the hole diffusion length is drawn in Fig. 38. The growth temperature was approximately  $674^\circ\text{C}$  and  $T_s$  was varied from  $781^\circ$  to  $721^\circ\text{C}$ . The longest  $L_p$  ( $5.5 \mu\text{m}$ ) was obtained at the highest  $T_s$  and decreased as  $T_s$  was reduced, at  $T_s = 721^\circ\text{C}$  the diffusion length was  $1.5 \mu\text{m}$ . The electron concentration of these layers was determined to be in the low  $10^{15} \text{ cm}^{-3}$  range. The scatter in the data is inexplicable at this time, but the trend in the data of decreasing  $L_p$  with decreasing  $T_s$  is definite. Since the diffusion length is longer for higher  $T_s$  it indicates a longer minority carrier lifetime and higher quality material. This effect may be attributed to a higher conversion efficiency of In to InCl due to the higher source temperature.

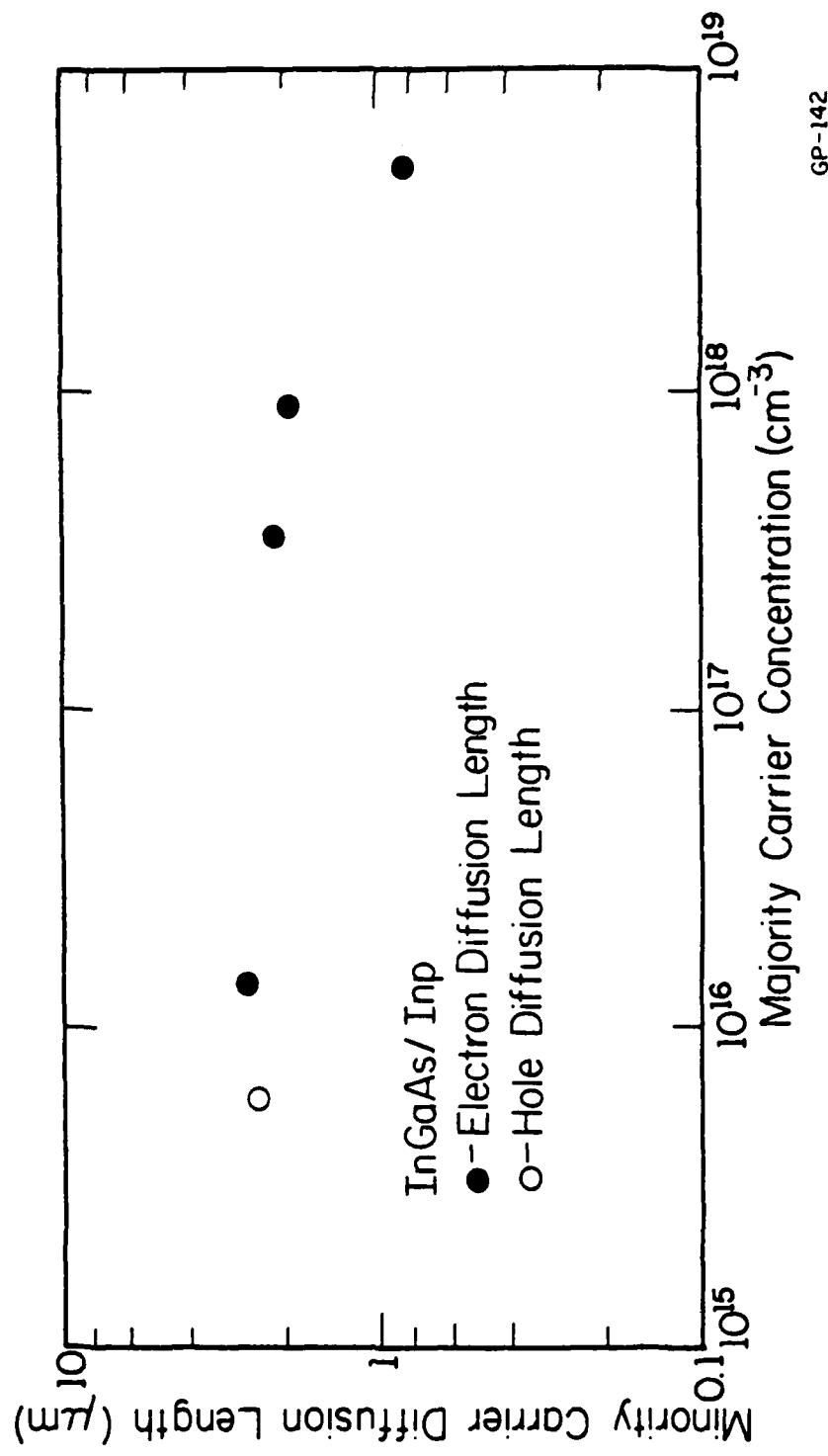


Figure 37. The variation of the electron diffusion length with hole concentration of InGaAs. Also shown is the hole diffusion length of an n-type InGaAs layer.

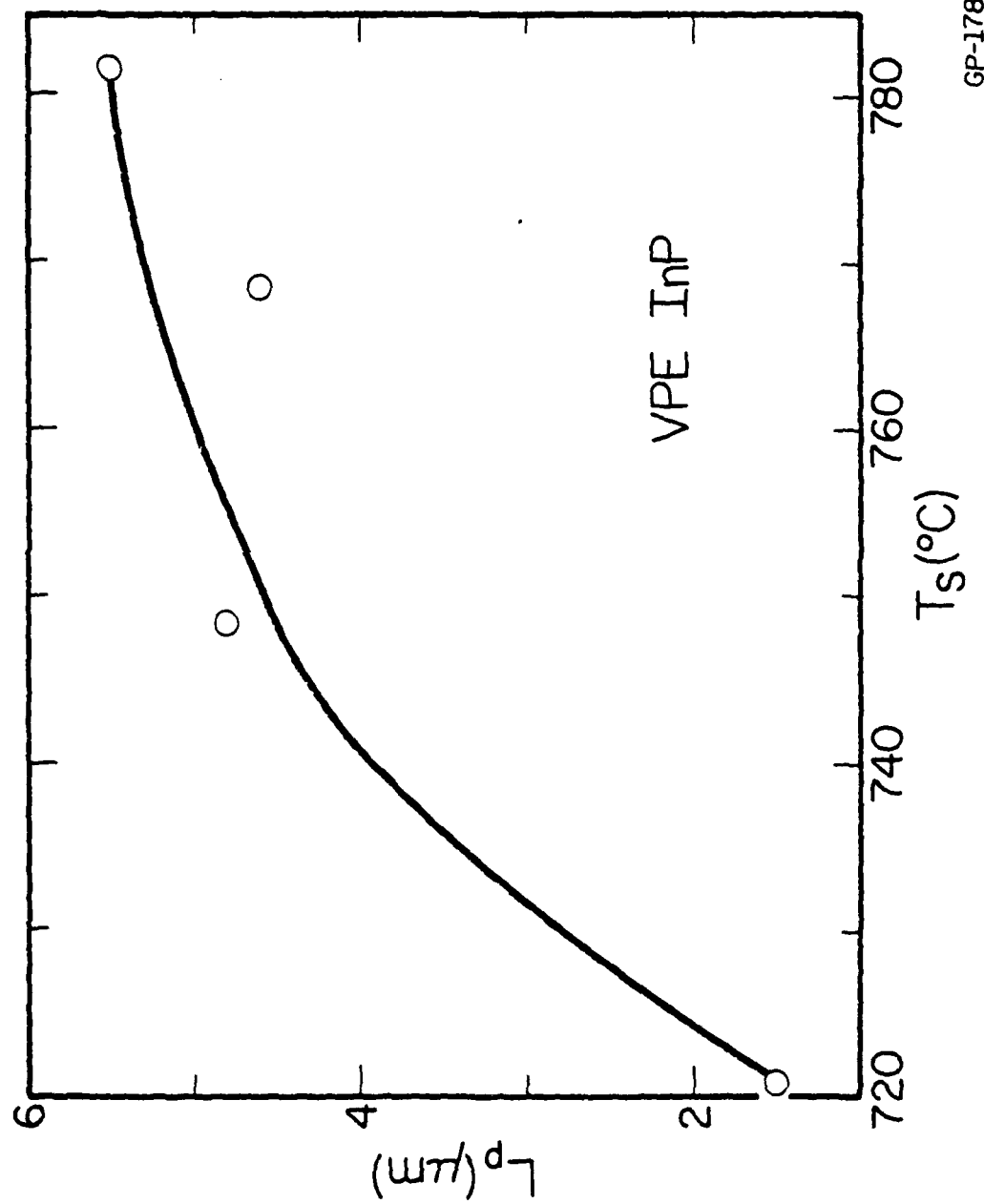


Figure 38. The effect of In boat source temperature on the hole diffusion lengths of VPE InP epitaxial layers.

## V. DISCUSSION AND CONCLUSIONS

### A. Characterization of LPE Growth

In the first part of this report, X-ray diffraction was used to characterize the LPE growth of InGaAsP and InGaAs epitaxial layers grown on InP substrates. The distribution coefficients for lattice matched growth of InGaAsP layers with bandgaps in the 1.15 to 1.31  $\mu\text{m}$  region were determined. Extrapolation of the distribution coefficient data in Fig. 7 has been helpful in the growth of longer wavelength ( $\lambda_g = 1.55 \mu\text{m}$ ) material.<sup>27</sup> The surface morphology of these layers was found to be more sensitive to lattice mismatch at the longer wavelength compositions. A detailed study of the effect of the melt composition on  $\lambda_g = 1.15 \mu\text{m}$  layers grown by step cooling was presented. It was found that both  $\Delta a/a$  and  $\lambda_g$  varied linearly with  $X_{\text{As}}^l$ ,  $\Delta a/a$  varied linearly, and  $\lambda_g$  was almost constant for changes in  $X_{\text{Ga}}^l$ , and both  $\Delta a/a$  and  $\lambda_g$  were constant with changes in  $X_{\text{P}}^l$ . Thus large changes in  $\Delta a/a$  and  $\lambda_g$  can be obtained with the variations of  $X_{\text{As}}^l$  and  $X_{\text{Ga}}^l$  while a change in  $\Delta a/a$  with little variation in  $\lambda_g$  can be obtained by varying  $X_{\text{Ga}}^l$ .

An important result was that both  $\Delta a/a$  and  $\lambda_g$  are affected by the growth temperature. Growth by techniques involving a cooling rate resulted in compositionally graded layers, and constant composition layers could be obtained with a constant growth temperature, i.e., step cooling.

Auger depth profiling was used to investigate the interfacial region of InGaAsP/InP and InGaAs/InGaAsP heterojunctions grown by LPE. It was found that significant grading at the interface is caused by lattice mismatch and that the high diffusivity of As in In solutions results in interface broadening of layers with a lower As content grown on layers with a higher As content, indicating that high bandgap on low bandgap heterostructures will be difficult to grow by LPE.

Future work should involve the use of a double crystal diffractometer because of its greater resolution and nearly ideal diffraction conditions. This instrument should allow a more thorough investigation of graded layers and allow for the quantitative determination of crystal quality through comparison with theoretical diffraction peak intensity predictions. The work presented here can also be extended to characterize the growth of VPE InGaAsP and InGaAs.

#### B. Minority Carrier Diffusion Lengths

The variation of the electron diffusion length with hole concentration for the quaternary and ternary are qualitatively the same with the main difference being the occurrence of the sharp drop-off in  $L_n$  occurring at a hole concentration an order of magnitude lower for the quaternary. In addition,  $L_n$  for the quaternary is longer than  $L_n$  for the ternary for the lightly doped samples while the reverse is observed at the higher doping levels. The qualitative behavior of  $L_n$  of these Zn-doped materials is similar to a previous study where the electron diffusion length was measured as a function of hole concentration in Ge-doped GaAs p-n junctions.<sup>28</sup> In the GaAs work, the gradual decrease in  $L_n$  with increasing hole concentration at low concentrations was attributed to the dominance of nonradiative recombination, while at the higher hole concentrations the rapid decrease in  $L_n$  is influenced by radiative recombination.

In the lattice mismatch experiment, the hole diffusion length of n-type InGaAsP was found to decrease linearly as the lattice mismatch increased in the range  $-0.25\% < \Delta a/a < 0.31\%$ . The longest value of  $L_p$  (1.5  $\mu\text{m}$ ) was obtained when the epitaxial layer was lattice matched to the substrate. Other workers have reported the thermal expansion coefficient of InGaAsP ( $\alpha_g = 1.3 \mu\text{m}$ )<sup>29</sup> and their data indicate that the layer lattice matched at

room temperature would be mismatched by approximately +0.06% at the growth temperature of 640°C used in this work. However, the data presented in this paper reveal that, when considering solely the diffusion length, the absence of strain (lattice mismatch) at room temperature is more important than the possible generation of misfit dislocations due to the small mismatch at the growth temperature for this particular composition of the quaternary. This indicates that any room temperature mismatch at the heterojunction interface degrades the bulk properties of the epitaxial layer. This conclusion is in qualitative agreement with other work done on severely mismatched ( $\Delta a/a = -3.7\%$ ) GaAs/GaP heterojunctions where it was found that the hole diffusion length in GaAs of the heterojunction samples was an order of magnitude shorter than that in GaAs homojunction (lattice matched) samples.<sup>30</sup>

The hole diffusion lengths of VPE InP was found to markedly decrease with decreasing source temperature. This result indicates that higher quality VPE InP is grown with a high  $T_s$ . It is suggested that a more efficient conversion of In to InCl is obtained at higher  $T_s$  resulting in better material.

Future work in this area should include more detailed studies of VPE material to determine the optimum growth conditions, gas flows and temperatures, for obtaining long diffusion lengths. The effects of interface recombination should be investigated as was done previously with a higher bandgap semiconductor grown on the beveled junction samples.<sup>31</sup> It appears that this can be accomplished only with VPE because of the previously mentioned dissolution problem in LPE growth.

## REFERENCES

1. G. A. Antypas, R. L. Moon, L. W. James, J. Edgecumbe and R. L. Bell, Gallium Arsenide and Related Compounds (Boulder) 1972 (Inst. Phys. Conf. Ser. No. 17), 48 (1973).
2. G. E. Stillman, IEDM Tech. Digest, 638 (1979).
3. M. M. Tashima, L. W. Cook, and G. E. Stillman, J. Cryst. Growth, 54, 132 (1981).
4. G. H. Stout and L. H. Jensen, X-ray Structure Determination. MacMillan, 410 (1968).
5. J. Matsui, K. Onabe, T. Kamejima and I. Hayashi, J. Electrochem. Soc. 126, 664 (1979).
6. K. Oe, Y. Shinoda and K. Sugiyama, Appl. Phys. Lett., 33, 962 (1978).
7. M. Feng, T. H. Windhorn, M. M. Tashima and G. E. Stillman, Appl. Phys. Lett., 32, 758 (1978).
8. M. Feng, M. M. Tashima, T. H. Windhorn, and G. E. Stillman, Appl. Phys. Lett., 33, 533 (1978).
9. M. Feng, L. W. Cook, M. M. Tashima and G. E. Stillman, J. Electron. Mater., 9, 241 (1980).
10. J. J. Hsieh, M. C. Finn and J. A. Rossi, Gallium Arsenide and Related Compounds (St. Louis) 1976 (Inst. Phys. Conf. Ser. No. 33b), 37 (1977).
11. M. Feng, L. W. Cook, M. M. Tashima, T. H. Windhorn and G. E. Stillman, Appl. Phys. Lett., 34, 292 (1979).
12. J. Burgeat, M. Quillec, J. Primot, G. LeRoux and H. Launois, Appl. Phys. Lett., 38, 542 (1981).
13. M. Feng, M. M. Tashima, L. W. Cook and G. E. Stillman, Gallium Arsenide and Related Compounds (St. Louis) 1978 (Inst. Phys. Conf. Ser. No. 45), 61 (1979).
14. M. Feng, M. M. Tashima, L. W. Cook, R. A. Milano, and G. E. Stillman, Appl. Phys. Lett., 34, 91 (1979).
15. M. Feng, L. W. Cook, M. M. Tashima, G. E. Stillman and R. J. Blattner, Appl. Phys. Lett., 34, 697 (1979).
16. L. W. Cook, M. Feng, M. M. Tashima, R. J. Blattner and G. E. Stillman, Appl. Phys. Lett., 37, 173 (1980).

17. C. M. Garner, Y. D. Shen, J. S. Kim, G. L. Pearson, W. E. Spicer, J. S. Harris and D. D. Edwall, J. Appl. Phys., 48, 3147 (1977).
18. H. Kressel and J. K. Butler, Semiconductor Lasers and Heterojunction LEDs. New York: Academic Press, 291, 1977.
19. L. W. Cook, M. M. Tashima and G. E. Stillman, Appl. Phys. Lett., 36, 904 (1980).
20. J. J. Loferski and J. J. Wysocki, RCA Rev., 22, 38 (1961).
21. L. M. Zinkiewicz, T. J. Roth, B. J. Skromme and G. E. Stillman, Gallium Arsenide and Related Compounds (Vienna) 1980 (Vienna) 1980 (Inst. Phys. Conf. Ser. No. 56), 19 (1981).
22. N. Holonyak, Jr., B. A. Vojak and R. M. Kolbas, Solid-State Electron., 22, 431 (1979).
23. C. E. Hurwitz and J. J. Hsieh, Appl. Phys. Lett., 32, 487 (1978).
24. G. H. Olsen and T. J. Zamerowski, IEEE J. Quantum Electron., QE-17, 128 (1981).
25. S. Sakai, M. Umeno and Y. Amemiya, Japan J. Appl. Phys., 19, 109 (1980).
26. Y. Takeda, M. Kuzuhara and A. Sasaki, Japan J. Appl. Phys., 19, 899 (1980).
27. L. W. Cook, Private communication.
28. H. C. Casey, Jr., B. I. Miller and E. Pinkas, J. Appl. Phys., 44, 1281 (1973).
29. R. Bisaro, P. Merenda, T. P. Pearsall, Appl. Phys. Lett., 34, 100 (1979).
30. M. L. Young and M. C. Rowland, Phys. Stat. Sol. (a), 16, 603 (1973).
31. M. Ettenberg and G. H. Olsen, J. Appl. Phys., 48, 4275 (1977).

## PUBLICATIONS SUPPORTED BY THIS CONTRACT

1. M. Feng, T. H. Windhorn, M. M. Tashima, and G. E. Stillman, "Liquid-phase epitaxial growth of lattice-matched InGaAsP on (100)-InP for the 1.15-1.31- $\mu$ m spectral region," Appl. Phys. Lett., 32, 758(1978).
2. M. Feng, M. M. Tashima, T. H. Windhorn, and G. E. Stillman, "Composition dependence of the influence of lattice mismatch on surface morphology in LPE growth of InGaAsP on (100)-InP," Appl. Phys. Lett., 33, 533(1978).
3. M. Feng, M. M. Tashima, L. W. Cook, R. A. Milano, and G. E. Stillman, "The influence of growth-solution dopants on distribution coefficients in the LPE growth of InGaAsP," Appl. Phys. Lett., 34, 91(1979).
4. M. Feng, M. M. Tashima, L. W. Cook, and G. E. Stillman, "Impurity dependence of distribution coefficients in the LPE growth of InGaAsP," 7th Intl. Svmp. on GaAs and Related Compounds, Institute Phys. Conf. Ser. No. 45 (London, 1979), pp. 61-70.
5. M. Feng, L. W. Cook, M. M. Tashima, T. H. Windhorn, and G. E. Stillman, "The influence of LPE growth techniques on the alloy composition of InGaAsP," Appl. Phys. Lett., 34, 292(1979).
6. M. Feng, L. W. Cook, M. M. Tashima, R. J. Blattner, and G. E. Stillman, "Auger profile study of the influence of lattice mismatch on the LPE InGaAsP-InP heterojunction interface," Appl. Phys. Lett., 34, 697(1979).
7. M. Feng, L. W. Cook, M. M. Tashima, and G. E. Stillman, "Lattice constant, bandgap, thickness, and surface morphology of InGaAsP-InP layers grown by step-cooling equilibrium-cooling, supercooling and two-phase-solution growth techniques," J. Electron. Mater., 9, 241(1980).
8. L. W. Cook, M. M. Tashima, and G. E. Stillman, "Effects of a finite melt on the thickness and composition of liquid phase epitaxial InGaAsP and InGaAs layers grown by the diffusion-limited step-cooling technique," Appl. Phys. Lett., 36, 904(1980).
9. L. W. Cook, M. Feng, M. M. Tashima, R. J. Blattner, and G. E. Stillman, "Interface grading in InGaAsP liquid phase epitaxial heterostructures," Appl. Phys. Lett., 37, 173(1980).
10. L. W. Cook, M. M. Tashima, and G. E. Stillman, "Variation of the thickness and composition of LPE InGaAsP, InGaAs, and InP layers grown from a finite melt by the step-cooling technique," J. Electron. Mater., 10, 119(1981).
11. M. M. Tashima, L. W. Cook, and G. E. Stillman, "The application of X-ray diffraction measurements in the growth of LPE InGaAsP/InP," J. Cryst. Growth, 54, 132(1981).
12. M. M. Tashima, L. W. Cook, N. Tabatabaie, and G. E. Stillman, "The effect of lattice mismatch on hole diffusion lengths in liquid phase epitaxial InGaAsP( $\lambda_g = 1.15 \mu\text{m}$ )/InP," Appl. Phys. Lett., 38, 1009(1981).

